

Bioinspired HOF-based luminescent skin sensor with triple mechanochromism responses for recognition and collection of human biophysical signals

Xin Xu,^a and Bing Yan^{*,a}

^a Shanghai Key Lab of Chemical Assessment and Sustainability, School of Chemical Science and Engineering, Tongji University, Siping Road 1239, Shanghai 200092, China. E-mail: byan@tongji.edu.cn.

Electronic supplementary information

Experimental Section

1. Materials
2. Physical Measurements
3. Preparation of HOF-TJ-1
4. Preparation of elastic porous HOF-TJ-1@PDMS film
5. Preparation of RhB@HOF-TJ-1 (R), AY@HOF-TJ-1 (G) and AY/RhB@HOF-TJ-1 (Y)
6. Preparation of elastic HOF-TJ-1/R@PDMS bilayer film (1)
7. Preparation of elastic HOF-TJ-1/Y@PDMS bilayer film (2)
8. Preparation of elastic HOF-TJ-1/G@PDMS bilayer film (3)
9. Preparation of elastic HOF-TJ-1@PDMS bilayer film (4)
10. The Anti-interference Measurement of Porous HOF-TJ-1@PDMS Film toward Volatile Organic Compounds and Artificial Sweat
11. Single-Crystal X-ray Diffraction Determination
12. Density Functional Theory (DFT) Calculation
13. Mechanical Simulation
14. Skin Sensor Array Model Simulation

Fig. S1. (a) Single molecule structure of **HOF-TJ-1**. (b) The angle between plane 1 (blue) and plane 2 (yellow) is 59.917°, the angle between plane 1 (blue) and plane 3 (green) is 55.213°, the angle between plane 2 (yellow) and plane 3 (green) is 68.908°. Plane 1: C8–C13 atoms; Plane 2: C1–C6 atoms; Plane 3: C14–C19 atoms.

Fig. S2. (a) Two BPA⁻ anions connected by two H₂O molecules *via* hydrogen bond interaction along *bc* plane. (b) Adjacent BPA⁻ anions linked by hydrogen bond forms a 1-D chain along *ac* plane. (c) Adjacent 1-D chain of BPA⁻ anions connect with each other to form a 2-D BPA⁻ layer based on hydrogen bond interaction along *ab* plane. (d–e) The polyline-type structure of separate BPA⁻ anion layer and TBA⁺ cation layer viewed along *a* axis. (f) The micropore structure with ca. 5.6 Å diameter between BPA⁻ anion and TBA⁺ cation viewed along *a* axis.

Fig. S3. (a) PXRD patterns of **HOF-TJ-1** indicating chemical stability of **HOF-TJ-1** immersed in H₂O, acetone, trichloromethane, tetrahydrofuran, alkaline (pH = 14) and acidic aqueous (pH = 1) solutions. (b) TG curve of **HOF-TJ-1**. (c) PXRD patterns of **HOF-TJ-1**, **R**, **Y** and **G**. (d) IR spectra of **HOF-TJ-1**, **R**, **Y** and **G**.

Fig. S4. (a–d) Photoluminescence quantum yield of **HOF-TJ-1** (60.43%), **R** (62.00%), **Y** (47.28%) and **G** (34.20%).

Fig. S5. (a) Fluorescence lifetime ($\lambda_{\text{em}} = 470$ nm) of **HOF-TJ-1**. (b) Excitation spectrum of **HOF-TJ-1** ($\lambda_{\text{em}} = 470$ nm). (c) LUMO (-1.757 eV) and HOMO (-5.820 eV) orbit distribution of **HOF-TJ-1**. (d) CIE coordinates of **HOF-TJ-1** (0.1692, 0.1353), **R** (0.5021, 0.2694), **Y** (0.347, 0.5033) and **G** (0.2246, 0.5075).

Fig. S6. Schematic image of energy transfer from S_1^{HOF} to S_1^{Dye} state.

Fig. S7. The side view of **1** with bilayer structure under 365 nm UV light, the thickness of top and bottom layers are respectively 2.0 and 1.0 mm.

Fig. S8. EDX spectrum of **HOF-TJ-1@PDMS** film demonstrating the element content of C (54.12%), Si (12.39%), O (32.84%) and N (0.65%).

Fig. S9. (a) The uniaxial stretching strain curves of **1–4**. (b) Uniaxial stretching strain cycle of four times of **1**.

Fig. S10. (a) SEM picture of porous **HOF-TJ-1@PDMS** film ($V_{\text{PDMS}}/V_{\text{H}_2\text{O}}/V_{\text{ethanol}} = 2/1/1$). (b) SEM picture of porous **HOF-TJ-1@PDMS** film ($V_{\text{PDMS}}/V_{\text{H}_2\text{O}}/V_{\text{ethanol}} = 1/0/0$).

Fig. S11. The luminescence chemical stability of porous **HOF-TJ-1@PDMS** film (a–b), **R@PDMS** film (c–d), **G@PDMS** film (e–f) and **Y@PDMS** film (g–h) after exposing in 12 volatile organic compounds such as ammonia, hydrochloric acid, methanol, acetic acid, amine, chloroform, formamide, nitrobenzene, formaldehyde, benzaldehyde, methylamine and diethylamine for 10 min, and immersing in artificial sweat for 10 min. The thermal stability of porous **HOF-TJ-1@PDMS** film (i–j), **R@PDMS** film (k–l), **G@PDMS** film (m–n) and **Y@PDMS** film (o–p) in 30–80 °C temperature range.

Fig. S12. (a) Emission spectra of **1** upon different stretching strains (0–100% strain, $\lambda_{\text{ex}} = 365$ nm). (b) Dependence of emission intensity of 470 and 586 nm peaks on stretching strain of **1**. (c) Calibration curve of I/I_0 at 586 nm toward $\log_{10}(\varepsilon)$ upon 0–100% strain for **1**. ($\lambda_{\text{ex}} = 365$ nm). (d) Dependence of ratio of I_{470}/I_{586} on stretching strain of **1**. (e) Calibration curve of $\log_{10}(I_{470}/I_{586})$ toward stretching strain upon 0–100% strain for **1**. ($\lambda_{\text{ex}} = 365$ nm). (f) CIE coordinates of **1** upon different stretching strains.

Fig. S13. (a) Emission spectra of **2** upon different stretching strains (0–100% strain, $\lambda_{\text{ex}} = 365$ nm). (b) Dependence of emission intensity of 470 and 586 nm peaks on stretching strain of **2**. (c) Dependence of ratio of I_{470}/I_{586} on stretching strain of **2**. (d) Luminescence pictures of **2** upon different stretching strains (0–100% strain, $\lambda_{\text{ex}} = 365$ nm). (e) CIE coordinates of **2** upon different stretching strains. (f) The stretching cycle experiment of **2**. (g) Calibration curve of I/I_0 at 586 nm toward stretching strain upon 0–100% strain for **2**. ($\lambda_{\text{ex}} = 365$ nm). (h) Calibration curve of I/I_0 at 586 nm toward stretching strain upon 0–100% strain for **2**. ($\lambda_{\text{ex}} = 365$ nm).

Fig. S14. (a) Emission spectra of **3** upon different stretching strains (0–100% strain, $\lambda_{\text{ex}} = 365$ nm). (b) Dependence of emission intensity of 470 and 517 nm peaks on stretching strain of **3**. (c) Dependence of ratio of I_{470}/I_{517} on stretching strain of **3**. (d) Luminescence pictures of **3** upon different stretching strains (0–100% strain, $\lambda_{\text{ex}} = 365$ nm). (e) CIE coordinates of **3** upon different stretching strains. (f) The stretching cycle experiment of **3**. (g) Calibration curve of I/I_0 at 470 nm toward stretching strain upon 0–100% strain for **3** ($\lambda_{\text{ex}} = 365$ nm). (h) Calibration curve of I/I_0 at 517 nm toward stretching strain upon 0–100% strain for **3** ($\lambda_{\text{ex}} = 365$ nm).

Fig. S15. (a) Emission spectra of **4** upon different stretching strains (0–100% strain, $\lambda_{\text{ex}} = 365$ nm). (b) Luminescence pictures of **4** upon different stretching strains (0–100% strain, $\lambda_{\text{ex}} = 365$ nm). (c) Calibration curve of I/I_0 at 470 nm toward stretching strain upon 0–100% strain for **4** ($\lambda_{\text{ex}} = 365$ nm). (d) The stretching cycle experiment of **4**.

Fig. S16. Microscope pictures of porous **HOF-TJ-1@PDMS** layer upon 0% (a) and 50% (b) stretching strains.

Fig. S17. Dependence of I/I_0 on stretching strain of **R@PDMS** film (0–100% strain).

Fig. S18. FES 2-D mechanics stretching model of side view upon 0, 10, 20, 30, 40, 60, 70, 80, 90 and 100% strain for **1**.

Fig. S19. (a) Transmittance spectra of porous HOF-TJ-1@PDMS film and porous PDMS film. (b) The variation of thickness and transparency for the porous HOF-TJ-1@PDMS (top) layer.

Fig. S20. (a) Emission spectra of **1** with 0–180° bending angle ($\lambda_{\text{ex}} = 365$ nm). (b) Dependence of emission intensity of 470 and 586 nm peaks on bending strain of **1**. (c) Calibration curve of I/I_0 at 586 nm toward $\log_{10}(\theta)$ with 0–180° bending angle for **1**. ($\lambda_{\text{ex}} = 365$ nm). (d) Dependence of ratio of I_{470}/I_{586} on bending strain of **1**. (e) Calibration curve of $\log_{10}(I_{470}/I_{586})$ toward bending strain with 0–180° bending angle for **1**. ($\lambda_{\text{ex}} = 365$ nm). (f) CIE coordinates of **1** upon different bending strains.

Fig. S21. (a) Emission spectra of **2** with 0–180° bending angle ($\lambda_{\text{ex}} = 365$ nm). (b) Dependence of emission intensity of 470 and 586 nm peaks on bending strain of **2**. (c) Dependence of ratio of I_{470}/I_{586} on bending strain of **2**. (d) CIE coordinates of **2** upon different bending strains. (e) Luminescence pictures of **2** with 0–180° bending angle ($\lambda_{\text{ex}} = 365$ nm). (f) The bending cycle experiment of **2**. (g) Calibration curve of I/I_0 at 586 nm toward $\log_{10}(\theta)$ with 0–180° bending angle ($\lambda_{\text{ex}} = 365$ nm) for **2**. (h) Calibration curve of I/I_0 at 586 nm toward bending strain with 0–180° bending angle ($\lambda_{\text{ex}} = 365$ nm) for **2**. ($\lambda_{\text{ex}} = 365$ nm).

Fig. S22. (a) Emission spectra of **3** with 0–180° bending angle ($\lambda_{\text{ex}} = 365$ nm). (b) Dependence of emission intensity of 470 and 517 nm peaks on bending strain of **3**. (c) Dependence of ratio of I_{470}/I_{517} on bending strain of **3**. (d) CIE coordinates of **3** upon different bending strains. (e) Luminescence pictures of **3** with 0–180° bending angle ($\lambda_{\text{ex}} = 365$ nm). (f) The bending cycle experiment of **3**. (g) Calibration curve of I/I_0 at 470 nm toward $\log_{10}(\theta)$ with 0–180° bending angle ($\lambda_{\text{ex}} = 365$ nm). (h) Calibration curve of I/I_0 at 517 nm toward bending strain with 0–180° bending angle ($\lambda_{\text{ex}} = 365$ nm).

Fig. S23. (a) Emission spectra of **4** with 0–180° bending angle ($\lambda_{\text{ex}} = 365$ nm). (b) Calibration curve of I/I_0 at 470 nm toward bending strain with 0–180° bending angle ($\lambda_{\text{ex}} = 365$ nm) for **4** ($\lambda_{\text{ex}} = 365$ nm). (c) Luminescence pictures of **4** with 0–180° bending angle ($\lambda_{\text{ex}} = 365$ nm). (d) The bending cycle experiment of **4**.

Fig. S24. Microscope pictures of porous HOF-TJ-1@PDMS layer with 0° (a) and 60° (b) bending angles.

Fig. S25. FES 2-D mechanics bending model of side view with 0°, 30°, 60° and 90° angles for **1**.

Fig. S26. Calibration curve of $(I - I_0)/I_0$ at 470 nm toward pressing strain under 0–40% press strain.

Fig. S27. The pressing cycle experiment of **1**.

Fig. S28. (a) Kinetic curves of 470 and 586 nm peaks demonstrating the change of emission intensity upon 0, 10, 20, 30, and 40% press strains for **2**. (b) Calibration curve of I/I_0 at 586 nm toward pressing strain under 0–40% press strain for **2**. ($\lambda_{\text{ex}} = 310$ nm). (c) Luminescence pictures of initial **2** and **2** pressed by a glass tube ($\lambda_{\text{ex}} = 310$ nm). (d) Kinetic curves of 470 nm peak demonstrating the change of emission intensity upon 0, 10, 20, 30, and 40% press strains for **3**. (e) Calibration curve of I/I_0 of 470 nm peak toward pressing strain upon 0–40% strain for **3** ($\lambda_{\text{ex}} = 310$ nm). (f) Luminescence pictures of initial **3** and **3** pressed by a glass tube ($\lambda_{\text{ex}} = 310$ nm). (g) Kinetic curves of 470 nm peak demonstrating the change of emission intensity upon 0, 10, 20, 30, and 40% press strains for **4**. (h) Calibration curve of I/I_0 of 470 nm peak toward pressing strain upon 0–40% strain for **4** ($\lambda_{\text{ex}} = 310$ nm). (i) Luminescence pictures of initial **4** and **4** pressed by a glass tube ($\lambda_{\text{ex}} = 310$ nm).

Fig. S29. FES 2-D mechanics pressing model of side view under 10% (a) and 20% (b) pressing strain for **1**.

Fig. S30. (a) Kinetic curves of 586 nm peaks demonstrating the change of emission intensity with 0°, 30°, 60°, 90° bending angles for finger bending motion luminescence sensing. (b) Dependence of $(I - I_0)/I_0$ of 586 nm peaks on bending angle with 0–90°. (c) Kinetic curves of 586 nm peaks

demonstrating the change of emission intensity with 90° bending angle for fast and slow finger bending motion. (d) Luminescence pictures of **1** stuck on a finger with 0°, 30°, 60°, 90° bending angles, and relative R.G.B. values at bending center of **1** for finger bending motion chroma sensing. (e) Dependence of R.G.B. values of **1** on bending angle with 0–90°. (f) Dependence of R/B value of **1** on bending angle with 0–90° for finger bending motion chroma sensing.

Fig. S31. PCNN model constructed based on PMC property of **1** for enhancing tactile signal. Following five equations (1–5) are used for signal enhancing.

Fig. S32. (a) Schematic image demonstrating the 60 × 60 array based on **1** as mechanoreceptor for collecting initial palm texture, and PCNN model using to enhancing palm texture signal. (b) 3-D palm texture model obtained by 60 × 60 array based on **1**. (c) Initial 2-D palm texture gray image transformed by 3-D palm texture model. (d) Enhanced 3-D palm texture model obtained by 60 × 60 array based on **1**. (e) Enhanced 2-D palm texture gray image transformed by 3-D palm texture model.

Fig. S33. Training curve of BPNN1 model, the ordinate value decreases to 0, suggesting the successful fitting of BPNN1 model.

Fig. S34. Training curve of BPNN2 model, the ordinate value decreases to 0, suggesting the successful fitting of BPNN2 model.

Table S1. An overall comparison of this work and other works about luminescent mechanochromism polymer materials. (“Yes” outside the black circle means that this result is existent; “No” inside the black circle means that this result is non-existent; SMC: Stretched mechanochromism; BMC: Bended mechanochromism; PMC: Pressed mechanochromism)

Table S2. The crystallographic data of **HOF-TJ-1**.

Table S3. Summary of fluorescence decay lifetime of **1**.

Table S4. Element contents of C, Si, O, and N in porous HOF-TJ-1@PDMS film.

Table S5. CIE coordinates of **1**, **2** and **3** with different stretched strains of 0, 20, 40, 60, 80 and 100% ($\lambda_{\text{ex}} = 365$ nm).

Table S6. Detection limits of **1–4** in stretching, bending and pressing process.

Table S7. CIE coordinates of **1**, **2** and **3** with different bending angles of 0, 30, 60, 90, 120, 150 and 180° ($\lambda_{\text{ex}} = 365$ nm).

Table S8. CIE coordinates of **1** with different press strains of 0, 10, 20, 30 and 40%.

Table S9. Summary of input and output information during the training of BPNN1 for classifying bending angle (θ_1).

Table S10. Network structure information of BPNN1.

Table S11. The summary of mean square error (MSE), original value (OV), calculated value (CV), variance (Var.) for BPNN1.

Table S12. The matlab code of this BPNN 1.

Table S13. Summary of input and output information during the training of BPNN2.

Table S14. Network structure information of BPNN2.

Table S15. The summary of mean square error (MSE), original value (OV), calculated value (CV), variance (Var.) of BPNN2.

Table S16. The matlab code of this BPNN2.

Table S17. Summary data of the initial 3-D fingerprint texture image before tactile enhancement.

Table S18. Summary data of the initial 2-D fingerprint texture gray image before tactile enhancement.

Table S19. Summary data of the 3-D fingerprint texture image after tactile enhancement.

Table S20. Summary data of the 2-D fingerprint texture gray image after tactile enhancement.

Table S21. Summary data of the 3-D palm texture image before tactile enhancement.

Table S22. Summary data of the initial 2-D palm texture gray image before tactile enhancement.

Table S23. Summary data of the 3-D palm texture image after tactile enhancement.

Table S24. Summary data of the 3-D palm texture gray image after tactile enhancement.

Movie 1. Triple mechanochromism responses.

Movie 2. Finite element simulation.

Experimental Section

1. Materials

4,5-bis(4-carboxyphenyl)phthalic acid (BPA), tetrabutyl ammonium chloride (TBAC), polydimethylsiloxane (PDMS), Rhodamine B (RhB) and acridine yellow (AY) were all purchased from Sigma-Aldrich and used without further purification.

2. Physical Measurements

Powder X-ray diffraction (PXRD) patterns were collected with a Bruker D8 ADVANCE diffractometer using Cu $\text{K}\alpha$ radiation at 40 mA and 40 kV. SEM was performed on a Hitachi S-4800 field emission scanning electron microscope operating at 3 kV. TG curve was collected on a Bruker Tensor-II TGA 55 under the N₂ atmosphere with a heating rate of 10°C from 30 to 800°C. Energy dispersive X-ray spectroscopy (EDX) and the EDX mapping image were obtained by the scanning electron microscope operating at 15 kV. Fourier transform infrared (FT-IR) spectrum were recorded using a Nicolet IS10 infrared spectrophotometer. The photoluminescence (PL) emission, excitation spectra, PL quantum yield, and kinetics scan curve were recorded on an Edinburgh FLS920 spectrophotometer with a 450 W xenon lamp as an excitation source. Fluorescence lifetime measurement was measured on the Edinburgh FLS920 spectrophotometer with a laser.

In the measurement process of stretched-MC, **1** was clamped with two tweezers, a tweezer was fixed on a side of the sample platform, the other tweezer was connected with a nylon bandage. The nylon bandage was fixed on the other side of the sample platform, and the length of nylon bandage can be regulated to regulate the stretched strain (0-100%) of **1**. There is a length scale on sample platform. The sample platform was self-made. The sample platform was putted into the sample storehouse of Edinburgh FLS920 spectrophotometer for collecting PL emission spectra.

In the measurement process bended-MC, **1** was clamped with two tweezers, a tweezer was fixed on a side of the sample platform, the other tweezer was connected with a nylon bandage. A wire as center rotation axis was inserted at the bend center of **1** on the sample platform. The nylon bandage can rotate a certain angle (0-180°) to regulate the bend angle of **1**, and a pattern of protractor was drawn on the sample platform for determining the rotate angle. The sample platform was self-made. The sample platform was putted into the sample storehouse of Edinburgh FLS920 spectrophotometer for collecting PL emission spectra.

In the measurement process of pressed-MC, **1** was sandwiched by two glass slides, the distance of two glass slides can be regulated by using two elastic bands to bind two sides of the two glass slides. The two glass slides with **1** were putted into the sample storehouse of Edinburgh FLS920 spectrophotometer for collecting PL emission spectra. For kinetics curves measurement, **1** was sandwiched by two glass slides, two small elastic sponges were also sandwiched on two sides of the two glass slides. The two glass slides were bound by scotch tape on two sides. The distance of two glass slides can be regulated by using a glass tube to press the glass slides, two small elastic sponges can promote the recovery of distance between two glass slides. The point light is need to be aimed at the center of **1**. The incandescent lamp in room should be turned off.

For measuring the finger bend, **1** was stuck on the finger joint, then put the finger into the UV light source (point light, 50 W xenon lamp) of Edinburgh FLS920 spectrophotometer. The incandescent lamp in room should be turned off. Under the UV light source (point light, 50 W xenon lamp) of Edinburgh FLS920 spectrophotometer, the PL emission intensity of 586 nm peak

was measured by using kinetic curve measurement to monitor the finger bend, the point light is need to be aimed at the center of **1** on finger, and hand is need to remain stable.

3. Preparation of HOF-TJ-1

4,5-bis(4-carboxyphenyl)phthalic acid (BPA, 0.406 g, 0.001 mol) and tetrabutyl ammonium chloride (TBAC, 0.278 g, 0.001 mol) were mixed into a 20 mL methanol/H₂O (volume ratio = 1 : 19) solution to form a mixture, which was treated with ultrasound for 15 min. After the mixture was evaporated for about 24 h at room temperature, colourless and plate-like crystal can be acquired. Yield: 0.577 g, *ca.* 84.3%. Elemental analysis (%) calcd: C, 68.55; O, 21.63; N, 2.10. Found: C, 69.23; O, 22.15; N, 1.36.

4. Preparation of elastic porous HOF-TJ-1@PDMS film

0.002 g **HOF-TJ-1** was evenly dispersed in 1.00 ml of water/ethanol (1 : 1) mixed solution, which was then mixed with 1.1 ml PDMS solution (PDMS : curing agent = 10 : 1) to form a HOF-TJ-1@PDMS mixture. The HOF-TJ-1@PDMS mixture was put into a 25 mL beaker, which was exposed in atmospheric environment for 12 h. Afterwards, the HOF-TJ-1@PDMS mixture in beaker was heated in a 70 °C oven for 1 h. After taking out and cooling the beaker, the elastic porous HOF-TJ-1@PDMS film (thickness: *ca.* 2 mm) can be separated from the beaker.

5. Preparation of RhB@HOF-TJ-1 (R**), AY@HOF-TJ-1 (**G**) and AY/RhB@HOF-TJ-1 (**Y**)**

0.100 g **HOF-TJ-1** was mixed in 20 mL RhB aqueous solution (C = 0.0001 mol/L) to form a mixture, which was stirred for 10 h. Then pink RhB@HOF-TJ-1 (**R**) solid can be separated through centrifugation, filtration and drying.

The preparation of AY@HOF-TJ-1 (**G**) with green emission light is similarly with that of **R**, except that the 20 mL RhB aqueous solution (C = 0.0001 mol/L) is replaced by 20 mL acridine yellow aqueous solution (C = 0.0001 mol/L).

The preparation of AY/RhB@HOF-TJ-1 (**Y**) with yellow emission light is similarly with that of **R**, except that the 20 mL RhB aqueous solution (C = 0.0001 mol/L) is replaced by 20 mL RhB/acridine yellow aqueous solution (C = 0.0001 mol/L, n_{RhB}/n_{acridine yellow} = 2 : 3).

6. Preparation of elastic HOF-TJ-1/R@PDMS bilayer film (1**)**

0.01 g **R** powder was mixed evenly with 0.55 ml PDMS solution (PDMS : curing agent = 10 : 1) to form a R@PDMS mixture, which was poured into a rectangular plastic mold (1.0 × 2.0 cm²). The beaker was heated at 80 °C for 20 min, which resulted in a R@PDMS film. Afterwards, the HOF-TJ-1@PDMS mixture was coated on the upper surface of R@PDMS film evenly in the mold, which was exposed in atmospheric environment for 12 h. The mold was heated in a 70 °C oven for 30 min. After taking out and cooling the film, the elastic HOF-TJ-1/R@PDMS bilayer film (**1**) can be acquired.

7. Preparation of elastic HOF-TJ-1/Y@PDMS bilayer film (2**)**

The preparation of elastic HOF-TJ-1/Y@PDMS bilayer film (**2**) is similarly with that of **1**, except that 0.01 g **R** powder is replaced by 0.01 g **Y** powder.

8. Preparation of elastic HOF-TJ-1/G@PDMS bilayer film (3**)**

The preparation of elastic HOF-TJ-1/Y@PDMS bilayer film (**3**) is similarly with that of **1**, except that 0.01 g **R** powder is replaced by 0.01 g **G** powder.

9. Preparation of elastic HOF-TJ-1@PDMS bilayer film (4**)**

0.005 g **HOF-TJ-1** was evenly dispersed in 0.5 mL of water/ethanol (1 : 1) mixed solution, which was then mixed with 1.1 ml PDMS solution (PDMS : curing agent = 10 : 1) to form a HOF-TJ-1@PDMS mixture. Then 1 mL HOF-TJ-1@PDMS mixture was dopped in a rectangular plastic mold (1.0 × 2.0 cm²). The plastic mold was heated at 80 °C for 30 min, during the heating, the generated pores in the mixture should be punctured, which resulted in a HOF-TJ-1@PDMS film. Afterwards, 1.1 mL PDMS solution (PDMS : curing agent = 10 : 1) was mixed with 0.73 mL water/ethanol (1 : 1) mixed solution to form a white PDMS mixture, which was then coated on the upper surface of HOF-TJ-1@PDMS film evenly in the plastic mold. The plastic mold was exposed in atmospheric environment for 12 h. Then the breaker was heated in a 70 °C oven for 30 min. After taking out and cooling the film, the elastic HOF-TJ-1@PDMS bilayer film (**4**) can be acquired.

10. The Anti-interference Measurement of Porous HOF-TJ-1@PDMS Film toward Volatile Organic Compounds and Artificial Sweat

After exposing the porous HOF-TJ-1@PDMS film in a series of volatile organic compounds such as ammonia, hydrochloric acid, methanol, acetic acid, amine, chloroform, formamide, nitrobenzene, formaldehyde, benzaldehyde, methylamine and diethylamine for 10 min, respectively, the emission spectra of HOF-TJ-1@PDMS film were measured and compared with blank.

The artificial sweat was prepared by dissolving NaCl, KCl, Na₂SO₄, NH₄Cl, and ascorbic acid into aqueous solution with concentration of 40, 2.5, 1.2, 4.5 and 0.03 mmol/L, respectively. After immersing HOF-TJ-1@PDMS film in the artificial sweat for 10 min, the emission spectrum of HOF-TJ-1@PDMS film was measured and compared with blank.

11. Single-Crystal X-ray Diffraction Determination

The crystallographic data of **HOF-TJ-1** was collected at 77 K on a Bruker Apex II diffractometer (D8 VENTURE) equipped with CCD two-dimensional detector fitted with Mo K α radiation (λ = 0.71073 Å). Through using the program SADABS, the multi-scan absorption corrections and routine Lorentz polarization were triumphantly acquired. The structure was solved with the Bruker ShelXT3 structure solution program using Intrinsic Phasing. Then using Olex2,¹ the structure was refined with the ShelXL5 refinement package using Least Square minimization. Anisotropic thermal parameters were used for the non-hydrogen atoms. H atoms attached to carbon and hydroxyl oxygen atoms were positioned geometrically and constrained to ride on their parent atoms. Crystal data as well as the details of data collection and refinements for the complexes are summarized in [Table S1](#). The supplementary crystallographic data for **HOF-TJ-1** (CCDC 2210794) can be found free of charge from the Cambridge Crystallographic Data Center via www.ccdc.cam.ac.uk/data_request/cif.

Reference

- [1] O. V. Dolomanov, L. J. Bourhis, R. J. Gildea, J. A. K. Howard, H. J. Puschmann, *Appl. Cryst.* **2009**, *42*, 339–341.

12. Density Functional Theory (DFT) Calculation

The density functional theory (DFT) calculation was carried to optimize molecule structure of **HOF-TJ-1** by using Gaussian 16W package based on B3LYP/6-31G basis group and method. The HUMO-LUMO of **HOF-TJ-1** molecule was acquired by inputting *chk*. files of optimized structure into GaussView 6.0 package.

13. Mechanical Simulation

Finite element simulation is implemented by using COMSOL Multiphysics 6.0 software. Structure mechanics module is employed to construct all simulation models. For building all simulation models, solid mechanics and porous elastic solid mechanics are set as physical fields. For stretched, bended and pressed mechanochromism, four 2-D porous PDMS skin models are constructed with stretched, bended and pressed deformation processes, respectively. The pore diameter in all PDMS skin models is set as 0.586 mm. For parameter generation of intrinsic physical property of PDMS material, density (ρ) is 970 kg/m³, Young's modulus (E) is 750 kPa, and Poisson's ratio (nu) is 0.49. Appropriate stretched, bended and pressed strains are set to ensure stability of specified displacement. And suitable stress variation ranges are modulated for better observation of force change in deformation process.

14. Skin Sensor Array Model Simulation

In the 40×50 skin sensor array, each sensor based on **1** possesses the size of 0.04×0.04 cm². Each sensor was treated as a stress point, 40×50 stress points form the skin sensor array for fingerprint texture recognition. In the 60×60 skin sensor array, each sensor based on **1** possesses the size of 0.35×0.35 cm². Each sensor was treated as a stress point, 60×60 stress points form the skin sensor array for palm texture recognition. All $(I - I_0)/I_0$ values at each stress point can construct the 3-D texture images of fingerprint and palm. The optical noise was randomly added on none-stress points.

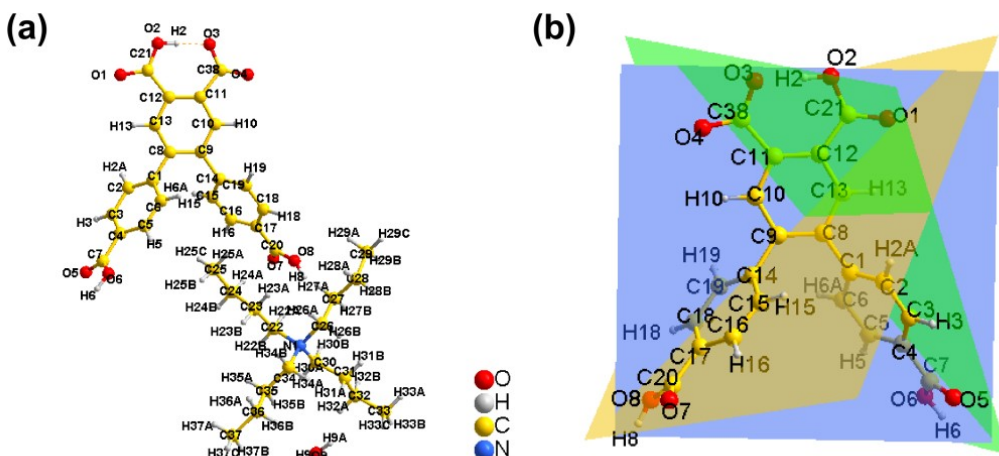


Fig. S1. (a) Single molecule structure of **HOF-TJ-1**. (b) The angle between plane 1 (blue) and plane 2 (yellow) is 59.917° , the angle between plane 1 (blue) and plane 3 (green) is 55.213° , the angle between plane 2 (yellow) and plane 3 (green) is 68.908° . Plane 1: C8–C13 atoms; Plane 2: C1–C6 atoms; Plane 3: C14–C19 atoms.

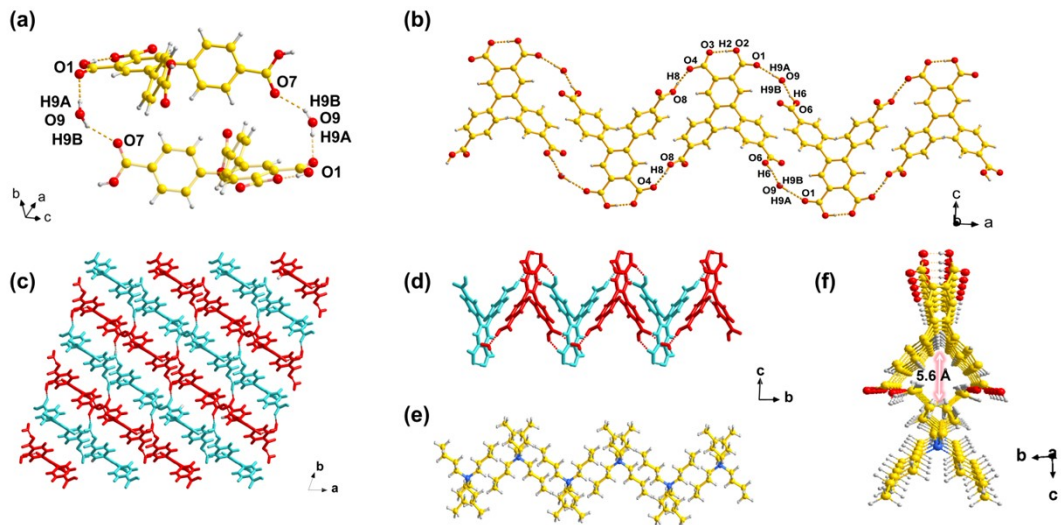


Fig. S2. (a) Two BPA^- anions connected by two H_2O molecules *via* hydrogen bond interaction along bc plane. (b) Adjacent BPA^- anions linked by hydrogen bond forms a 1-D chain along ac plane. (c) Adjacent 1-D chain of BPA^- anions connect with each other to form a 2-D BPA^- layer based on hydrogen bond interaction along ab plane. (d–e) The polyline-type structure of separate BPA^- anion layer and TBA^+ cation layer viewed along a axis. (f) The micropore structure with ca. 5.6 Å diameter between BPA^- anion and TBA^+ cation viewed along a axis.

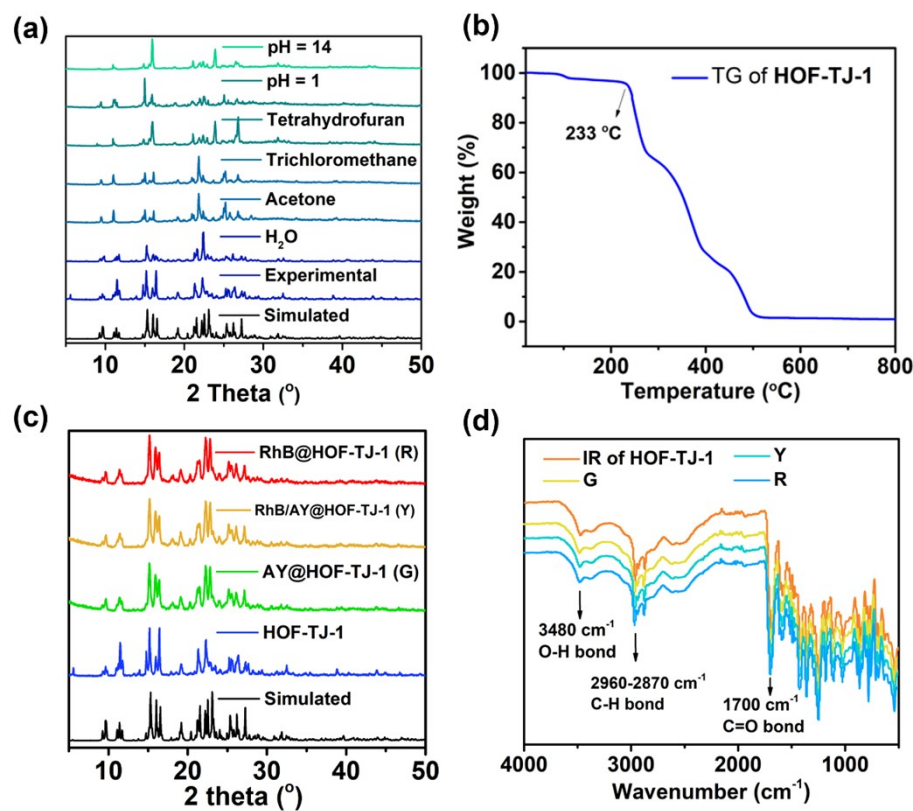


Fig. S3. (a) PXRD patterns of **HOF-TJ-1** indicating chemical stability of **HOF-TJ-1** immersed in H_2O , acetone, trichloromethane, tetrahydrofuran, alkaline ($\text{pH} = 14$) and acidic aqueous ($\text{pH} = 1$) solutions. (b) TG curve of **HOF-TJ-1**. (c) PXRD patterns of **HOF-TJ-1**, **R**, **Y** and **G**. (d) IR spectra of **HOF-TJ-1**, **R**, **Y** and **G**.

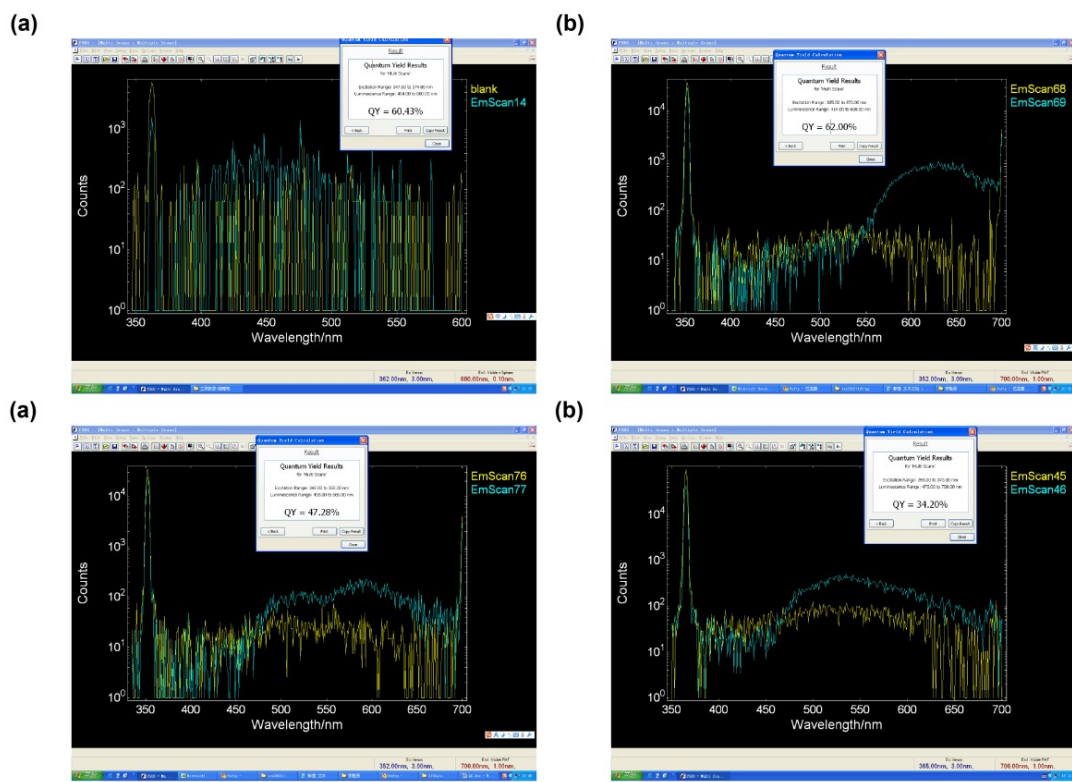


Fig. S4. (a-d) Photoluminescence quantum yield of **HOF-TJ-1** (60.43%), **R** (62.00%), **Y** (47.28%) and **G** (34.20%).

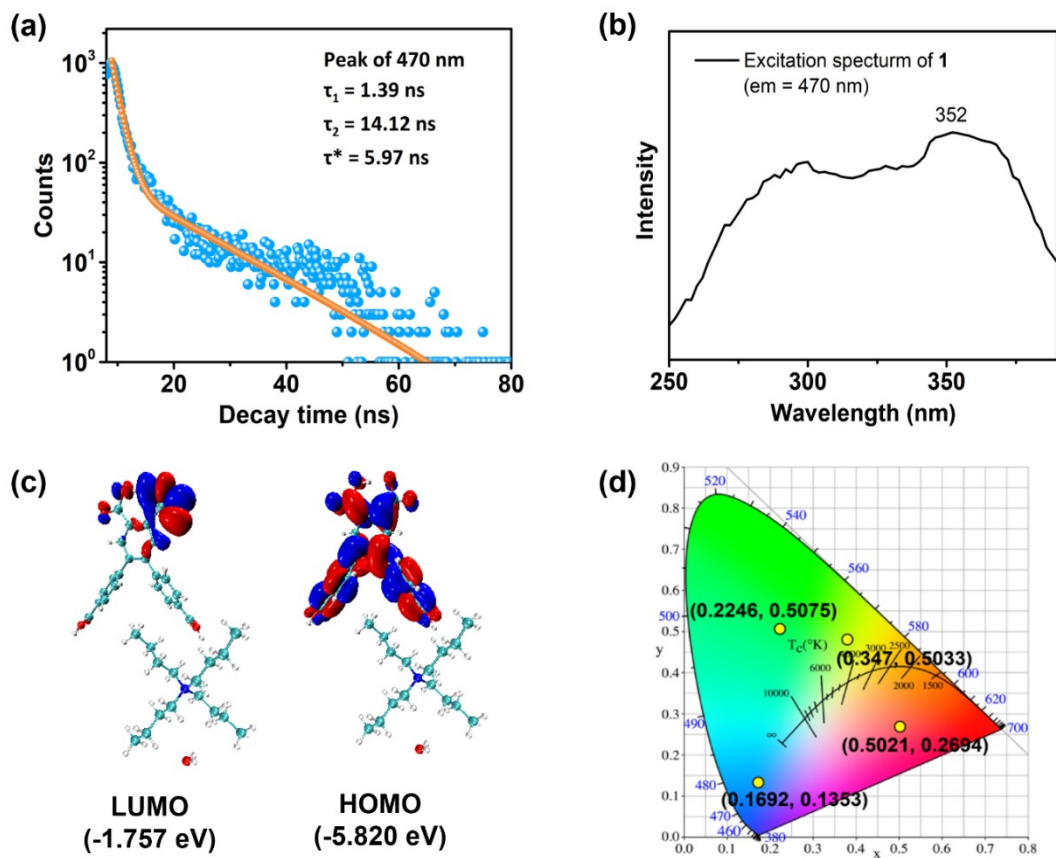


Fig. S5. (a) Fluorescence lifetime ($\lambda_{\text{em}} = 470$ nm) of **HOF-TJ-1**. (b) Excitation spectrum of **HOF-TJ-1** ($\lambda_{\text{em}} = 470$ nm). (c) LUMO (-1.757 eV) and HOMO (-5.820 eV) orbit distribution of **HOF-TJ-1**. (d) CIE coordinates of **HOF-TJ-1** ($0.1692, 0.1353$), **R** ($0.5021, 0.2694$), **Y** ($0.347, 0.5033$) and **G** ($0.2246, 0.5075$).

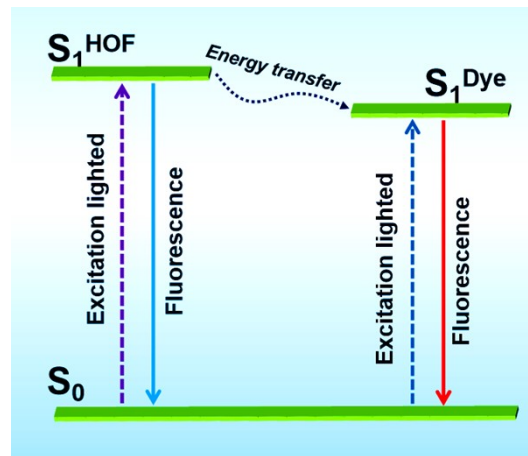


Fig. S6. Schematic image of energy transfer from S_1^{HOF} to S_1^{Dye} state.

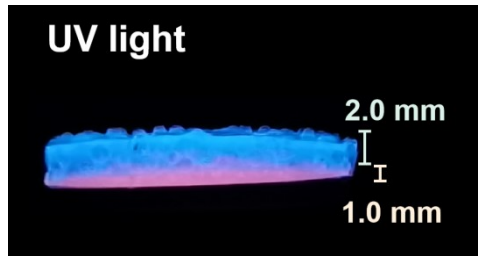


Fig. S7. The side view of **1** with bilayer structure under 365 nm UV light, the thickness of top and bottom layers are respectively 2.0 and 1.0 mm.

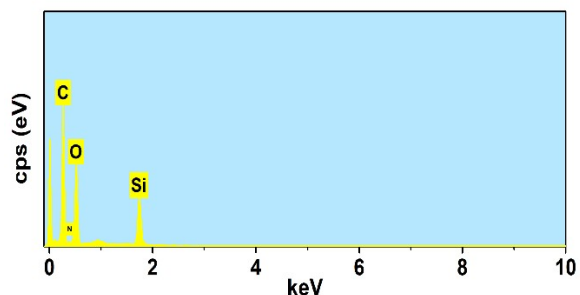


Fig. S8. EDX spectrum of HOF-TJ-1@PDMS film demonstrating the element content of C (54.12%), Si (12.39%), O (32.84%) and N (0.65%).

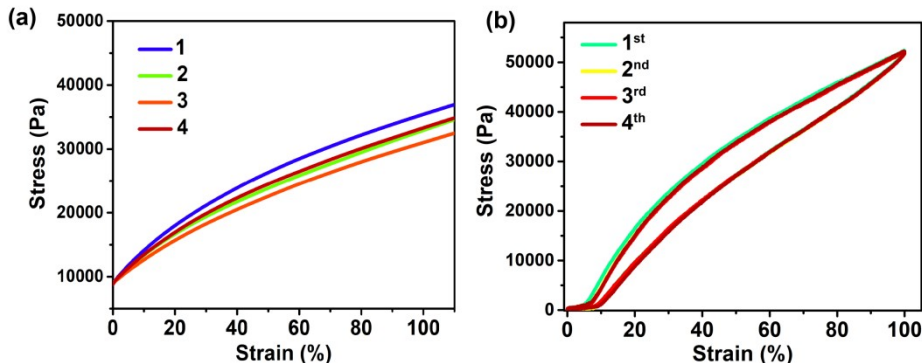


Fig. S9. (a) The uniaxial stretching strain curves of **1–4**. (b) Uniaxial stretching strain cycle of four times of **1**.

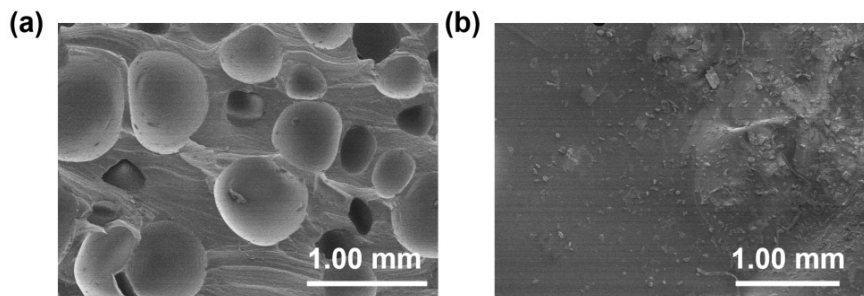


Fig. S10. (a) SEM picture of porous HOF-TJ-1@PDMS film ($V_{\text{PDMS}}/V_{\text{H}_2\text{O}}/V_{\text{ethanol}} = 2/1/1$). (b) SEM picture of porous HOF-TJ-1@PDMS film ($V_{\text{PDMS}}/V_{\text{H}_2\text{O}}/V_{\text{ethanol}} = 1/0/0$).

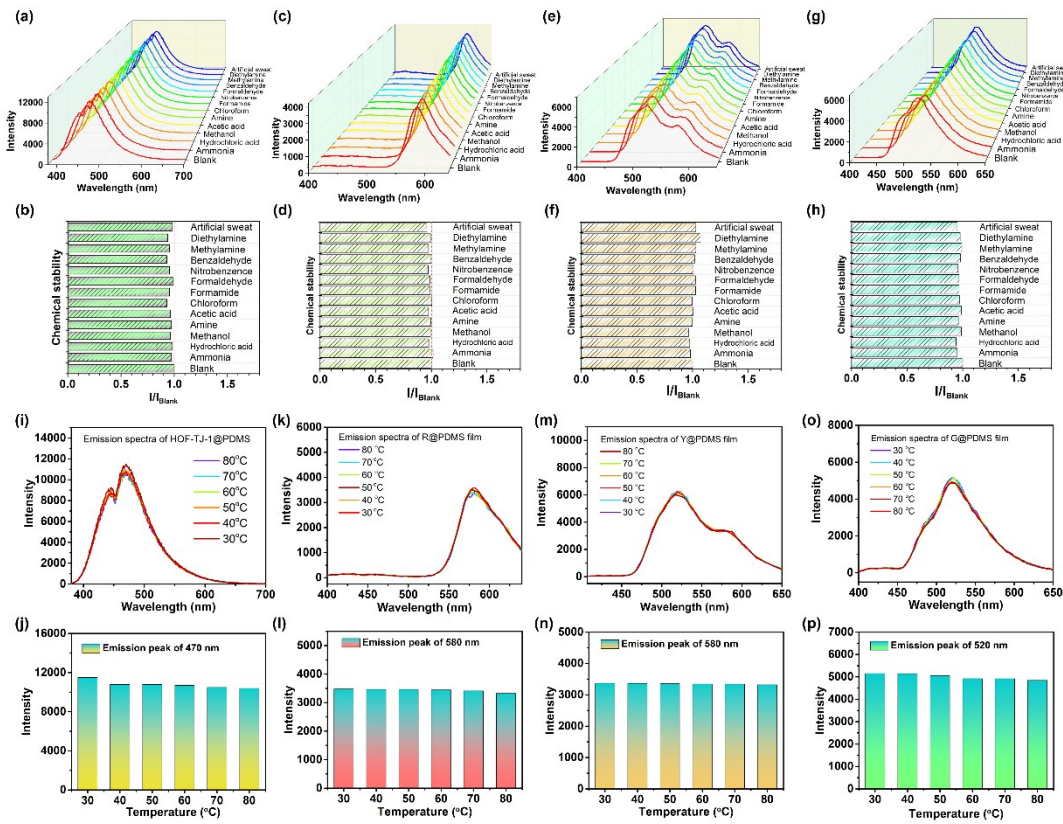


Fig. S11. The luminescence chemical stability of porous HOF-TJ-1@PDMS film (a–b), R@PDMS film (c–d), G@PDMS film (e–f) and Y@PDMS film (g–h) after exposing in 12 volatile organic compounds such as ammonia, hydrochloric acid, methanol, acetic acid, amine, chloroform, formamide, nitrobenzene, formaldehyde, benzaldehyde, methylamine and diethylamine for 10 min, and immersing in artificial sweat for 10 min. The thermal stability of porous HOF-TJ-1@PDMS film (i–j), R@PDMS film (k–l), G@PDMS film (m–n) and Y@PDMS film (o–p) in 30–80 °C temperature range.

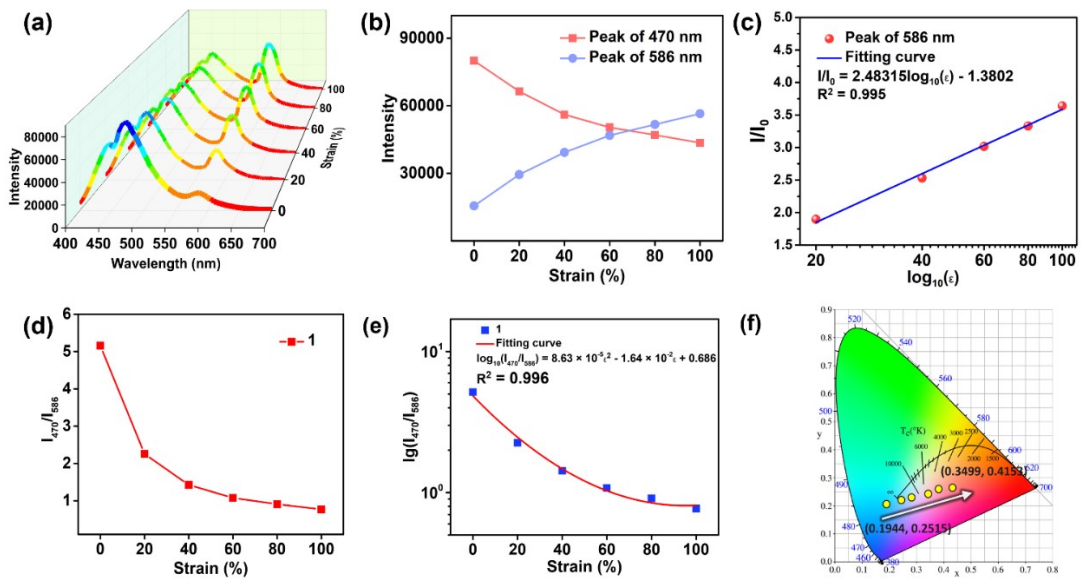


Fig. S12. (a) Emission spectra of **1** upon different stretching strains (0–100% strain, $\lambda_{\text{ex}} = 365$ nm). (b) Dependence of emission intensity of 470 and 586 nm peaks on stretching strain of **1**. (c) Calibration curve of I/I_0 at 586 nm toward $\log_{10}(\epsilon)$ upon 0–100% strain for **1**. ($\lambda_{\text{ex}} = 365$ nm). (d) Dependence of ratio of I_{470}/I_{586} on stretching strain of **1**. (e) Calibration curve of $\log_{10}(I_{470}/I_{586})$ toward stretching strain upon 0–100% strain for **1**. ($\lambda_{\text{ex}} = 365$ nm). (f) CIE coordinates of **1** upon different stretching strains.

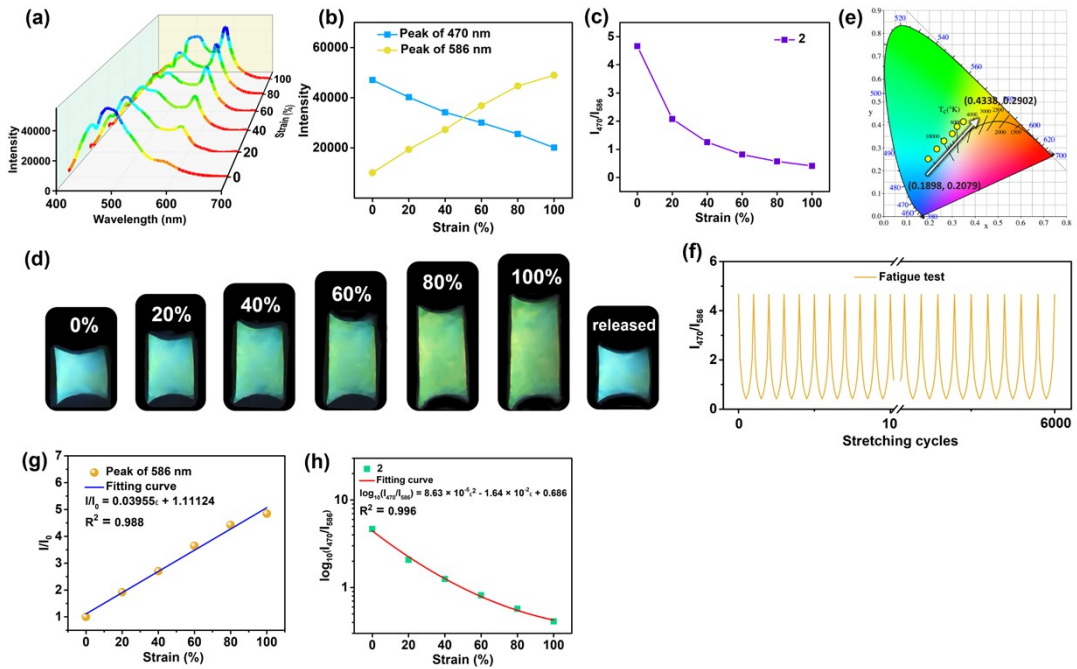


Fig. S13. (a) Emission spectra of **2** upon different stretching strains (0–100% strain, $\lambda_{\text{ex}} = 365 \text{ nm}$). (b) Dependence of emission intensity of 470 and 586 nm peaks on stretching strain of **2**. (c) Dependence of ratio of I_{470}/I_{586} on stretching strain of **2**. (d) Luminescence pictures of **2** upon different stretching strains (0–100% strain, $\lambda_{\text{ex}} = 365 \text{ nm}$). (e) CIE coordinates of **2** upon different stretching strains. (f) The stretching cycle experiment of **2**. (g) Calibration curve of I/I_0 at 586 nm toward stretching strain upon 0–100% strain for **2**. ($\lambda_{\text{ex}} = 365 \text{ nm}$). (h) Calibration curve of I/I_0 at 586 nm toward stretching strain upon 0–100% strain for **2**. ($\lambda_{\text{ex}} = 365 \text{ nm}$).

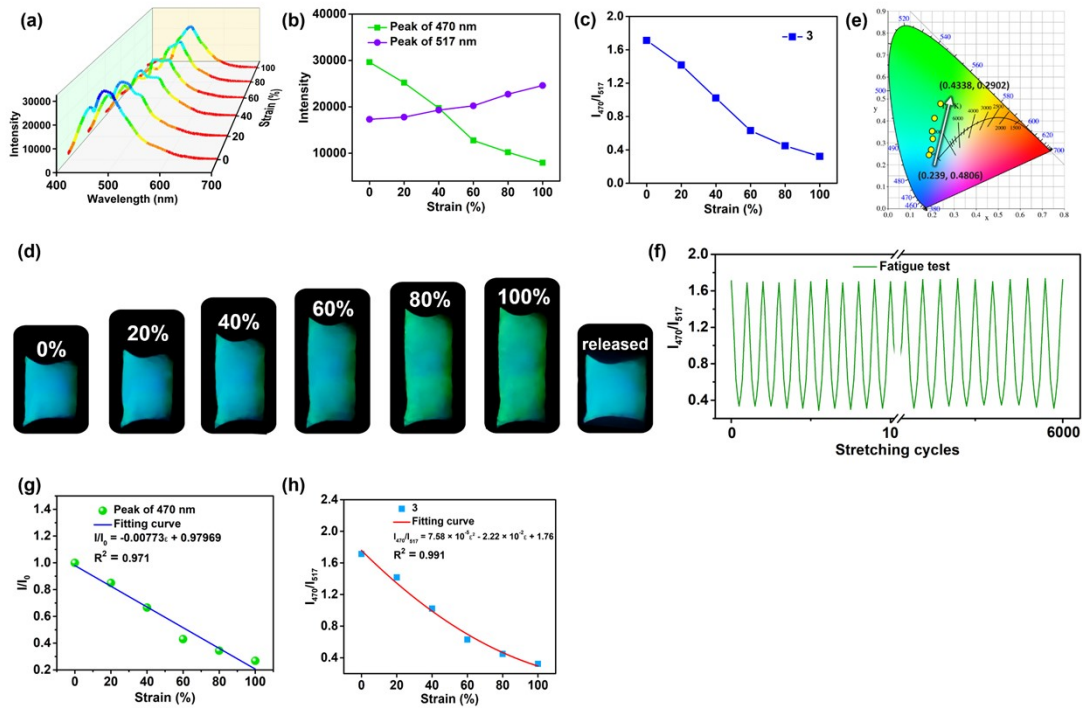


Fig. S14. (a) Emission spectra of **3** upon different stretching strains (0–100% strain, $\lambda_{\text{ex}} = 365 \text{ nm}$). (b) Dependence of emission intensity of 470 and 517 nm peaks on stretching strain of **3**. (c) Dependence of ratio of I_{470}/I_{517} on stretching strain of **3**. (d) Luminescence pictures of **3** upon different stretching strains (0–100% strain, $\lambda_{\text{ex}} = 365 \text{ nm}$). (e) CIE coordinates of **3** upon different stretching strains. (f) The stretching cycle experiment of **3**. (g) Calibration curve of I/I_0 at 470 nm toward stretching strain upon 0–100% strain for **3** ($\lambda_{\text{ex}} = 365 \text{ nm}$). (h) Calibration curve of I/I_0 at 517 nm toward stretching strain upon 0–100% strain for **3** ($\lambda_{\text{ex}} = 365 \text{ nm}$).

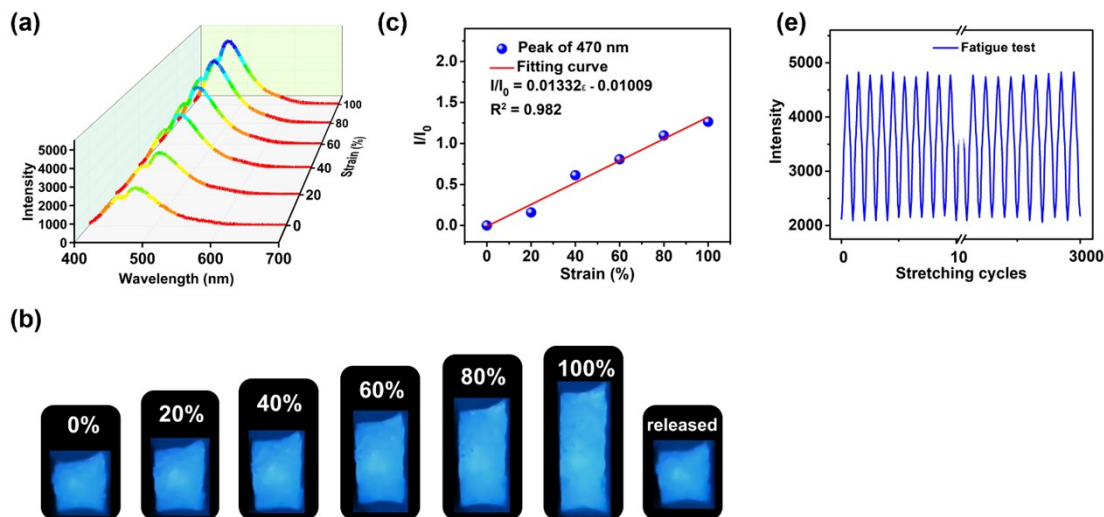


Fig. S15. (a) Emission spectra of **4** upon different stretching strains (0–100% strain, $\lambda_{\text{ex}} = 365 \text{ nm}$). (b) Luminescence pictures of **4** upon different stretching strains (0–100% strain, $\lambda_{\text{ex}} = 365 \text{ nm}$). (c) Calibration curve of I/I_0 at 470 nm toward stretching strain upon 0–100% strain for **4** ($\lambda_{\text{ex}} = 365 \text{ nm}$). (d) The stretching cycle experiment of **4**.

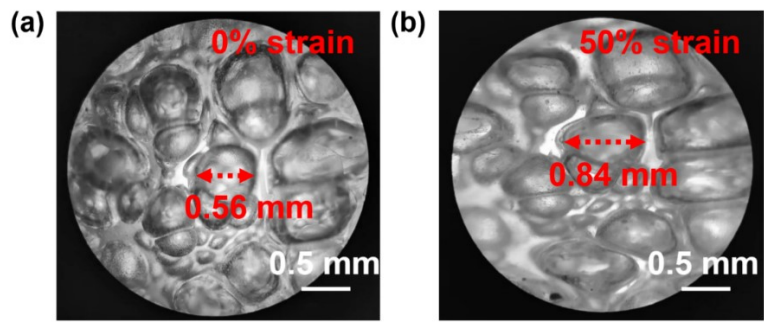


Fig. S16. Microscope pictures of porous HOF-TJ-1@PDMS layer upon 0% (a) and 50% (b) stretching strains.

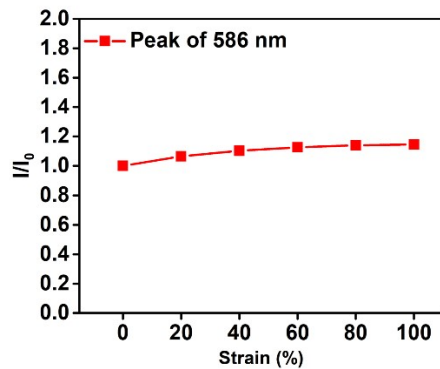


Fig. S17. Dependence of I/I_0 on stretching strain of R@PDMS film (0–100% strain).

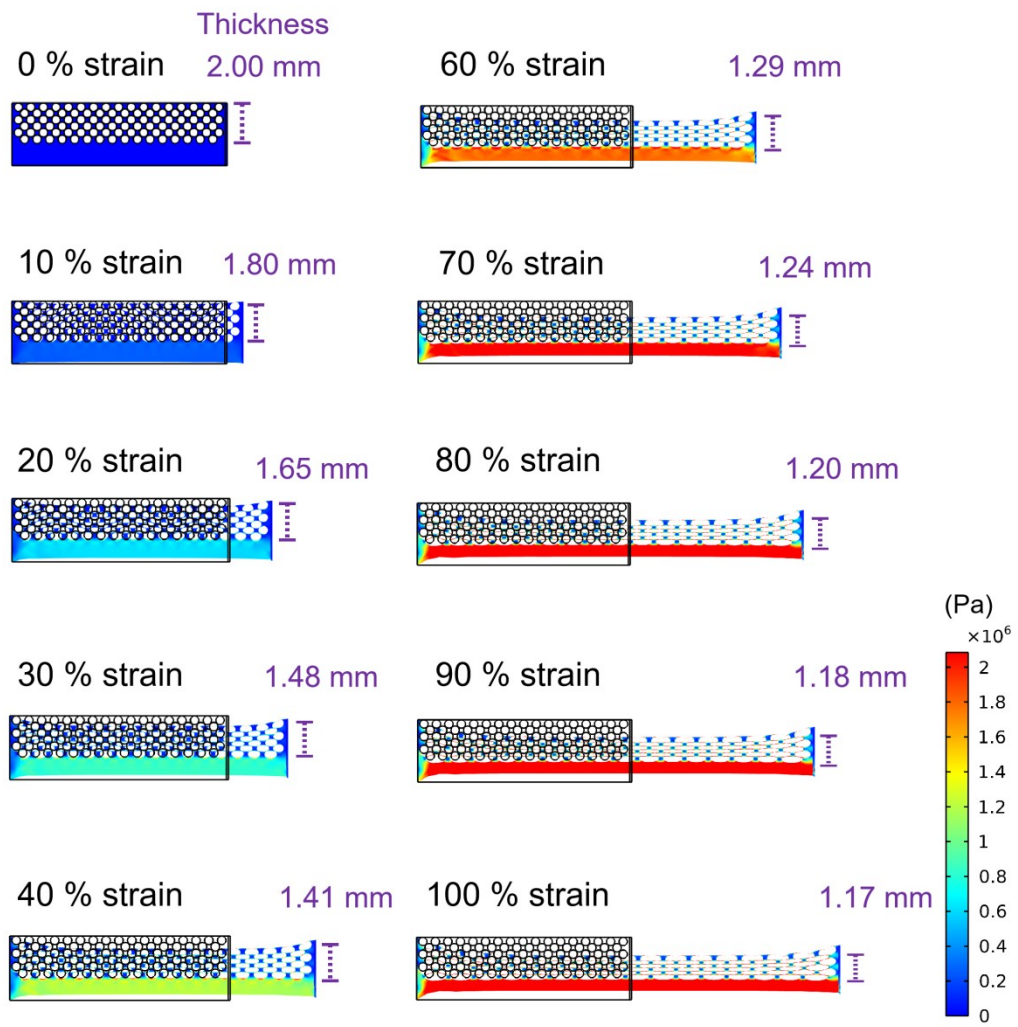


Fig. S18. FES 2-D mechanics stretching model of side view upon 0, 10, 20, 30, 40, 60, 70, 80, 90 and 100% strain for **1**.

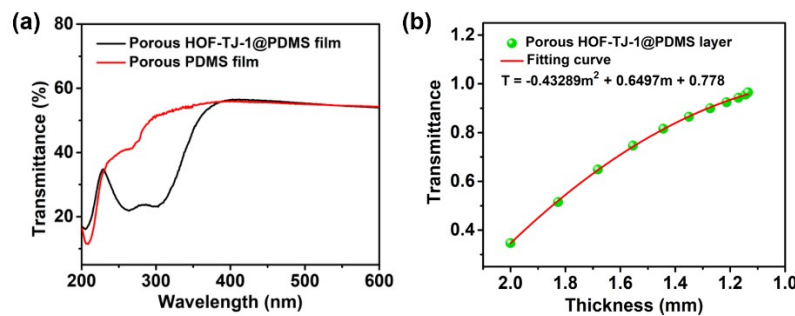


Fig. S19. (a) Transmittance spectra of porous HOF-TJ-1@PDMS film and porous PDMS film. (b) The variation of thickness and transparency for the porous HOF-TJ-1@PDMS (top) layer.

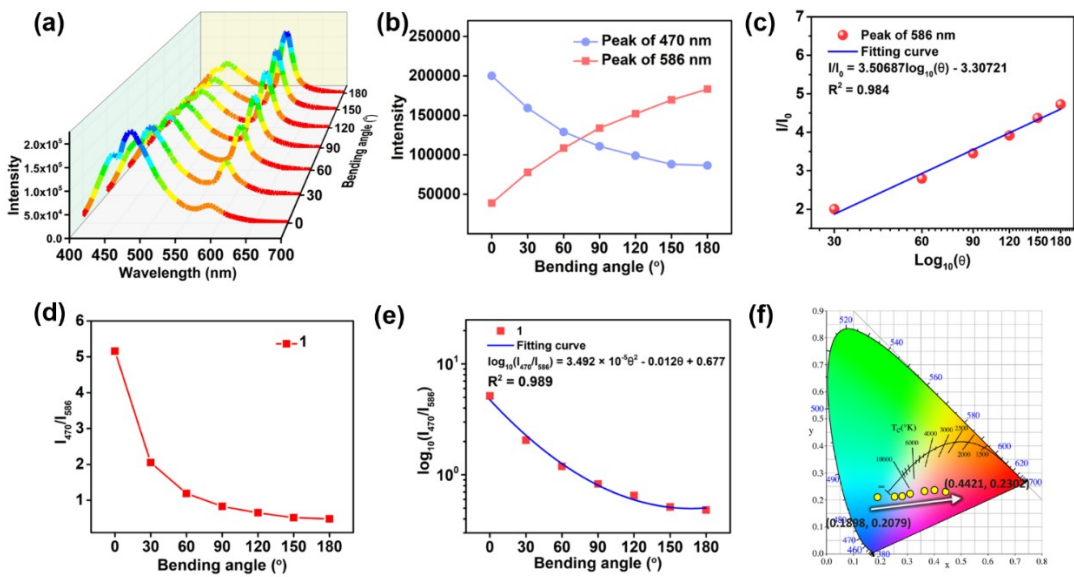


Fig. S20. (a) Emission spectra of **1** with 0–180° bending angle ($\lambda_{\text{ex}} = 365$ nm). (b) Dependence of emission intensity of 470 and 586 nm peaks on bending strain of **1**. (c) Calibration curve of I/I_0 at 586 nm toward $\log_{10}(\theta)$ with 0–180° bending angle for **1**. ($\lambda_{\text{ex}} = 365$ nm). (d) Dependence of ratio of I_{470}/I_{586} on bending strain of **1**. (e) Calibration curve of $\log_{10}(I_{470}/I_{586})$ toward bending strain with 0–180° bending angle for **1**. ($\lambda_{\text{ex}} = 365$ nm). (f) CIE coordinates of **1** upon different bending strains.

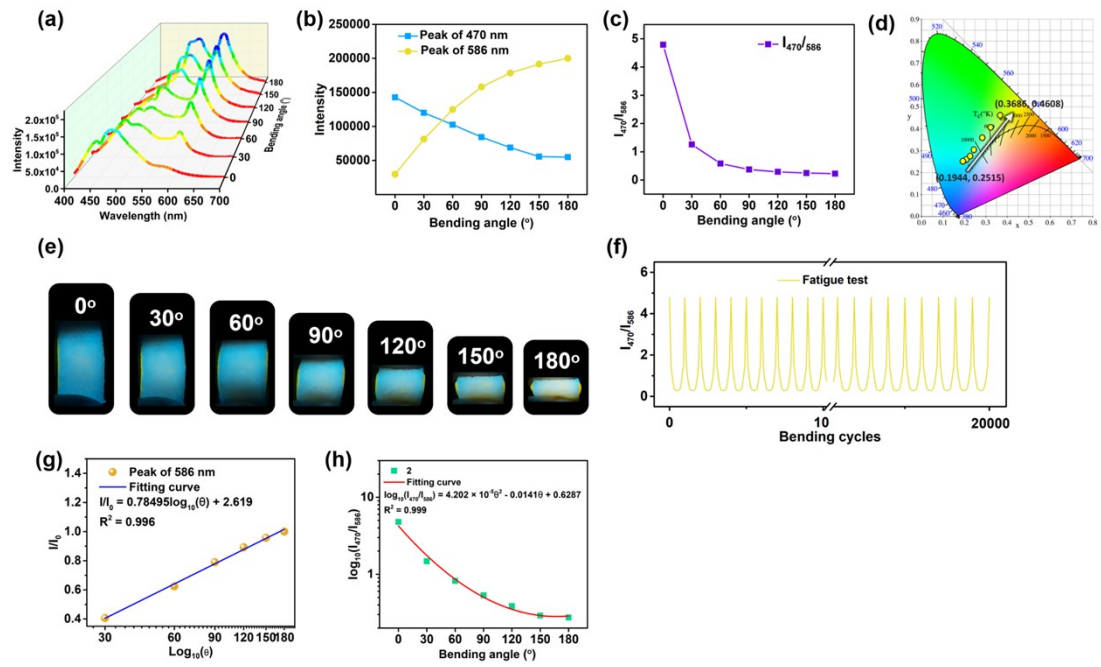


Fig. S21. (a) Emission spectra of **2** with 0–180° bending angle ($\lambda_{\text{ex}} = 365$ nm). (b) Dependence of emission intensity of 470 and 586 nm peaks on bending strain of **2**. (c) Dependence of ratio of I_{470}/I_{586} on bending strain of **2**. (d) CIE coordinates of **2** upon different bending strains. (e) Luminescence pictures of **2** with 0–180° bending angle ($\lambda_{\text{ex}} = 365$ nm). (f) The bending cycle experiment of **2**. (g) Calibration curve of I/I_0 at 586 nm toward $\log_{10}(\theta)$ with 0–180° bending angle ($\lambda_{\text{ex}} = 365$ nm) for **2**. (h) Calibration curve of I/I_0 at 586 nm toward bending strain with 0–180° bending angle ($\lambda_{\text{ex}} = 365$ nm) for **2**. ($\lambda_{\text{ex}} = 365$ nm).

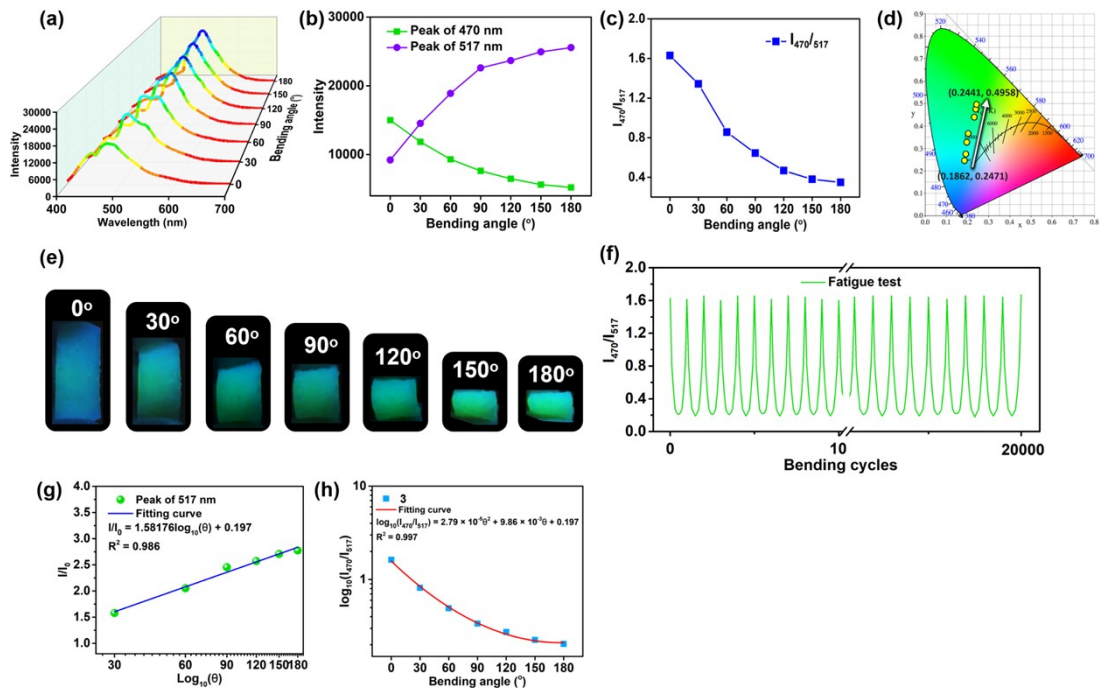


Fig. S22. (a) Emission spectra of **3** with 0–180° bending angle ($\lambda_{\text{ex}} = 365$ nm). (b) Dependence of emission intensity of 470 and 517 nm peaks on bending strain of **3**. (c) Dependence of ratio of I_{470}/I_{517} on bending strain of **3**. (d) CIE coordinates of **3** upon different bending strains. (e) Luminescence pictures of **3** with 0–180° bending angle ($\lambda_{\text{ex}} = 365$ nm). (f) The bending cycle experiment of **3**. (g) Calibration curve of I/I_0 at 470 nm toward $\log_{10}(\theta)$ with 0–180° bending angle ($\lambda_{\text{ex}} = 365$ nm). (h) Calibration curve of I/I_0 at 517 nm toward bending strain with 0–180° bending angle ($\lambda_{\text{ex}} = 365$ nm).

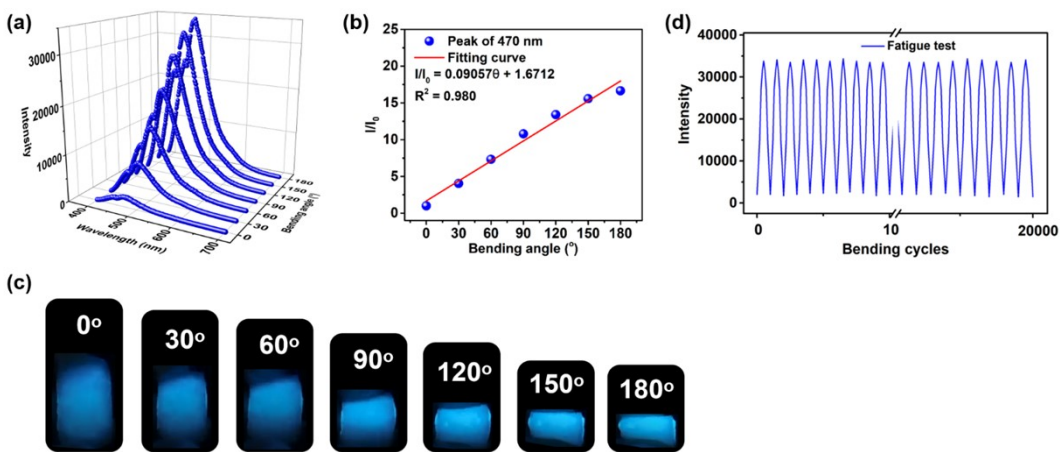


Fig. S23. (a) Emission spectra of **4** with 0–180° bending angle ($\lambda_{\text{ex}} = 365$ nm). (b) Calibration curve of I/I_0 at 470 nm toward bending strain with 0–180° bending angle ($\lambda_{\text{ex}} = 365$ nm) for **4** ($\lambda_{\text{ex}} = 365$ nm). (c) Luminescence pictures of **4** with 0–180° bending angle ($\lambda_{\text{ex}} = 365$ nm). (d) The bending cycle experiment of **4**.

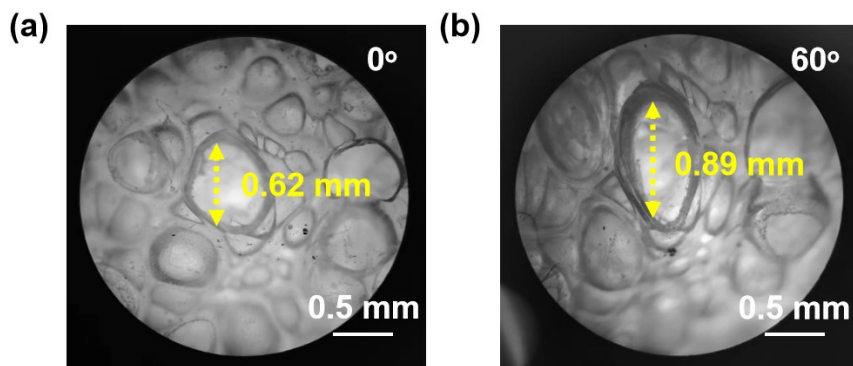


Fig. S24. Microscope pictures of porous HOF-TJ-1@PDMS layer with 0° (a) and 60° (b) bending angles.

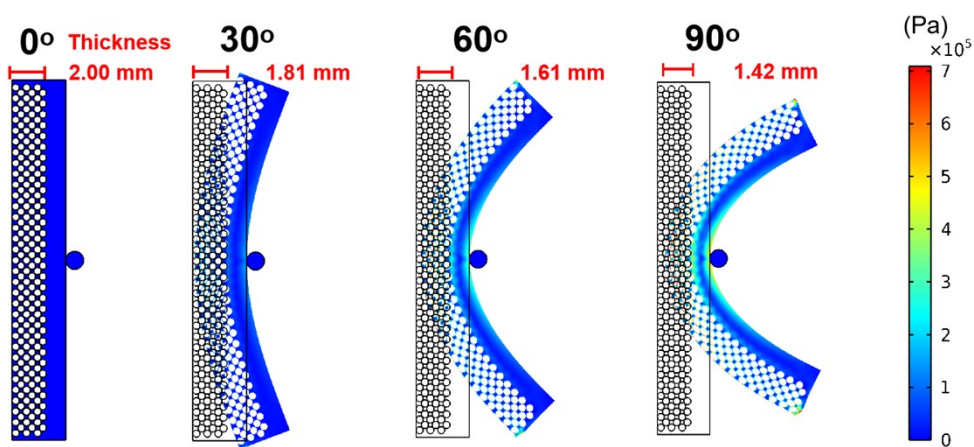


Fig. S25. FES 2-D mechanics bending model of side view with 0°, 30°, 60° and 90° angles for **1**.

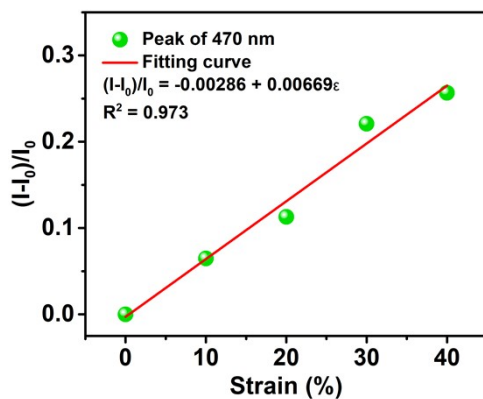


Fig. S26. Calibration curve of $(I - I_0)/I_0$ at 470 nm toward pressing strain under 0–40% press strain.

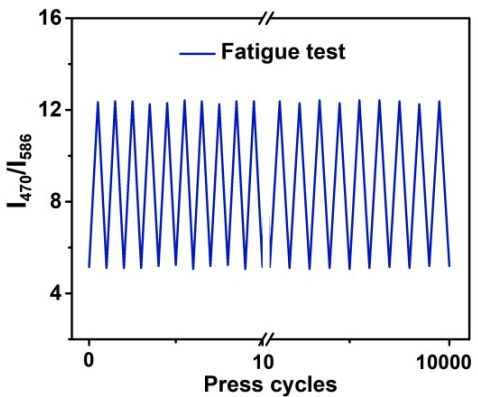


Fig. S27. The pressing cycle experiment of **1**.

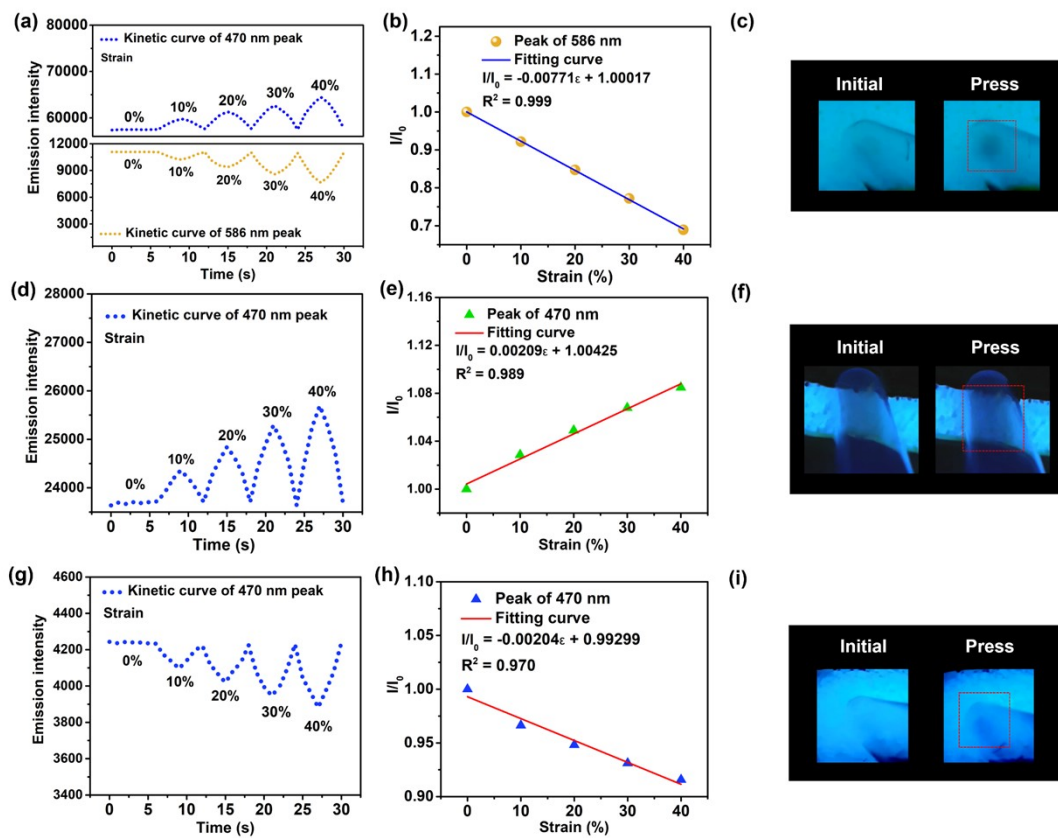


Fig. S28. (a) Kinetic curves of 470 and 586 nm peaks demonstrating the change of emission intensity upon 0, 10, 20, 30, and 40% press strains for **2**. (b) Calibration curve of I/I_0 at 586 nm toward pressing strain under 0–40% press strain for **2**. ($\lambda_{\text{ex}} = 310 \text{ nm}$). (c) Luminescence pictures of initial **2** and **2** pressed by a glass tube ($\lambda_{\text{ex}} = 310 \text{ nm}$). (d) Kinetic curves of 470 nm peak demonstrating the change of emission intensity upon 0, 10, 20, 30, and 40% press strains for **3**. (e) Calibration curve of I/I_0 of 470 nm peak toward pressing strain upon 0–40% strain for **3** ($\lambda_{\text{ex}} = 310 \text{ nm}$). (f) Luminescence pictures of initial **3** and **3** pressed by a glass tube ($\lambda_{\text{ex}} = 310 \text{ nm}$). (g) Kinetic curves of 470 nm peak demonstrating the change of emission intensity upon 0, 10, 20, 30, and 40% press strains for **4**. (h) Calibration curve of I/I_0 of 470 nm peak toward pressing strain upon 0–40% strain for **4** ($\lambda_{\text{ex}} = 310 \text{ nm}$). (i) Luminescence pictures of initial **4** and **4** pressed by a glass tube ($\lambda_{\text{ex}} = 310 \text{ nm}$).

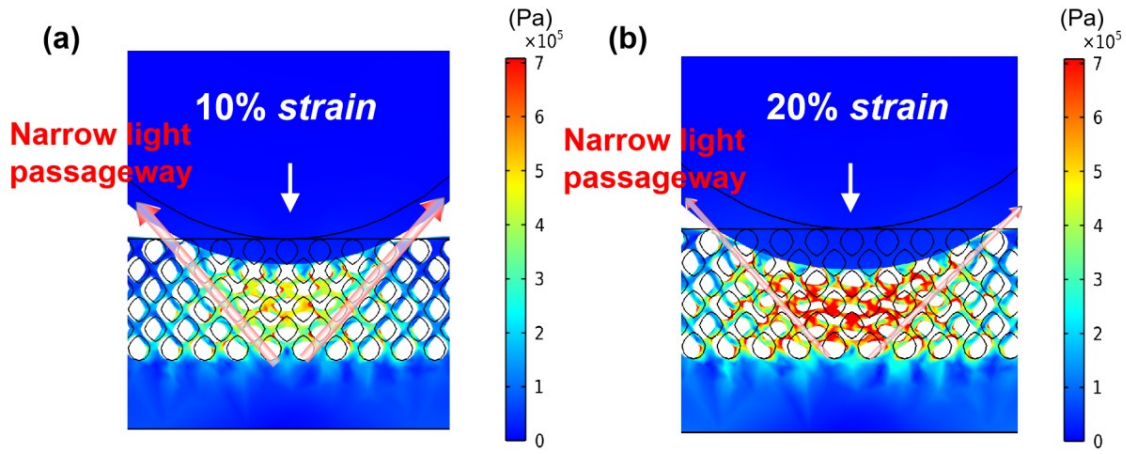


Fig. S29. FES 2-D mechanics pressing model of side view under 10% (a) and 20% (b) pressing strain for **1**.

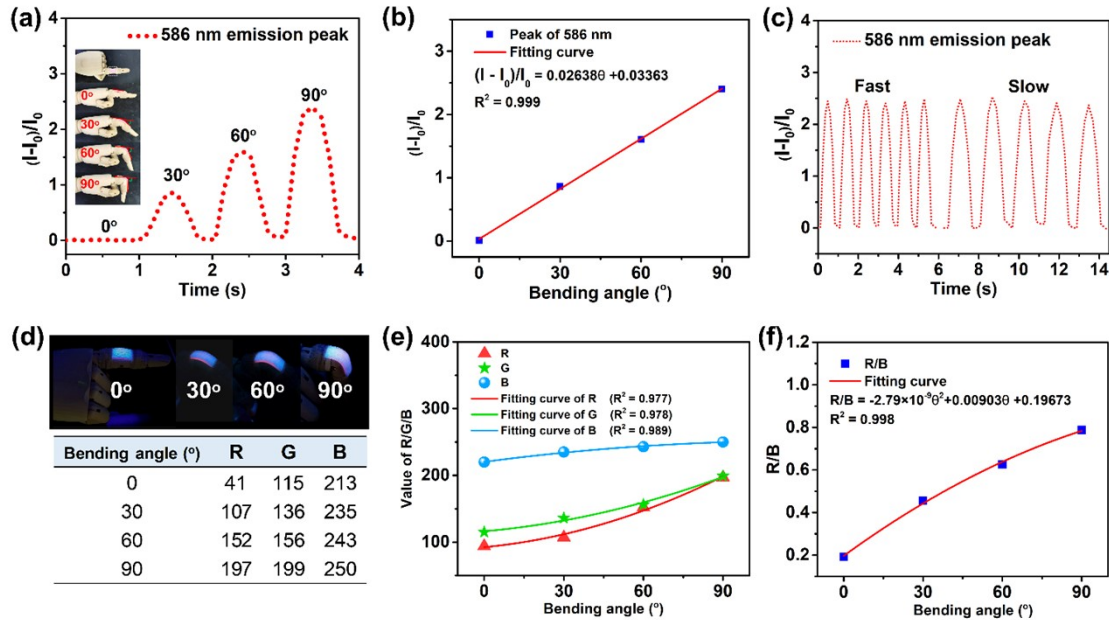


Fig. S30. (a) Kinetic curves of 586 nm peaks demonstrating the change of emission intensity with 0°, 30°, 60°, 90° bending angles for finger bending motion luminescence sensing. (b) Dependence of $(I - I_0)/I_0$ of 586 nm peaks on bending angle with 0–90°. (c) Kinetic curves of 586 nm peaks demonstrating the change of emission intensity with 90° bending angle for fast and slow finger bending motion. (d) Luminescence pictures of **1** stuck on a finger with 0°, 30°, 60°, 90° bending angles, and relative R.G.B. values at bending center of **1** for finger bending motion chroma sensing. (e) Dependence of R.G.B. values of **1** on bending angle with 0–90°. (f) Dependence of R/B value of **1** on bending angle with 0–90° for finger bending motion chroma sensing.

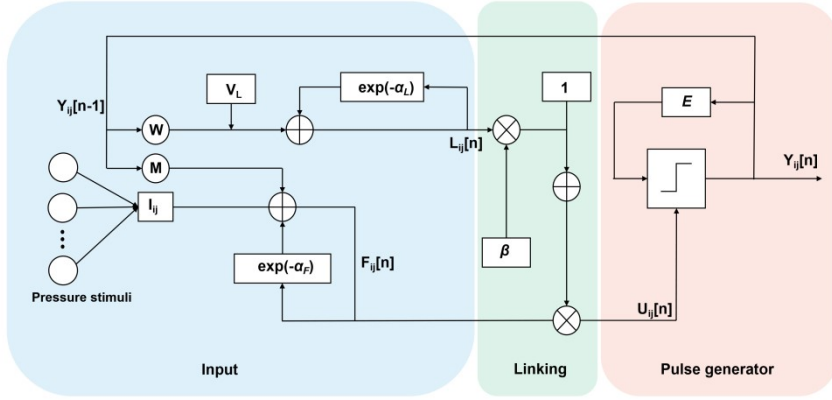


Fig. S31. PCNN model constructed based on PMC property of **1** for enhancing tactile signal. Following five equations (1–5) are used for signal enhancing.

$$F_{ij}[n] = e^{-\alpha_F} F_{ij}[n-1] + V_F \sum_k \omega_{ik} Y_{ik}[n-1] + I_{ij} \quad (1)$$

$$L_{ij}[n] = e^{-\alpha_L} L_{ij}[n-1] + V_L \sum_k m_{ik} Y_{ik}[n-1] \quad (2)$$

$$U_{ij}[n] = F_{ij}[n] + \eta + \beta_{ij} \eta \quad (3)$$

$$Y_{ij}[n] = \begin{cases} 1 & U_{ij}[n] > E_{ij}[n] \\ 0 & \text{else} \end{cases} \quad (4)$$

$$E_{ij}[n] = e^{-\alpha_E} E_{ij}[n-1] + V_E Y_{ij}[n] \quad (5)$$

The spiking encoded tactile information with various frequencies serves as I_{ij} at position (i, j) for the inputs of the PCNN. $F_{ij}[n]$ is the feedback input of the PCNN at (i, j) , and $L_{ij}[n]$ is the linking item. $U_{ij}[n]$ is the internal activity of PCNN, and $E_{ij}[n]$ is the dynamic threshold. The pulse output $Y_{ij}[n]$ is a binary value of either 0 or 1. The inter-connections of M and W are the constant synaptic weight matrices for the feeding and linking inputs, respectively. The value of matrix element $\omega_{ijk,l}$ and $m_{ijk,l}$ determine the synaptic weight strength for the synaptic weight matrices. α_F , α_L and α_E are the attenuation time constants of $F_{ij}[n]$, $L_{ij}[n]$ and $E_{ij}[n]$, respectively. V_F , V_L and V_E are the inherent voltage potentials of $F_{ij}[n]$, $L_{ij}[n]$ and $E_{ij}[n]$, respectively.

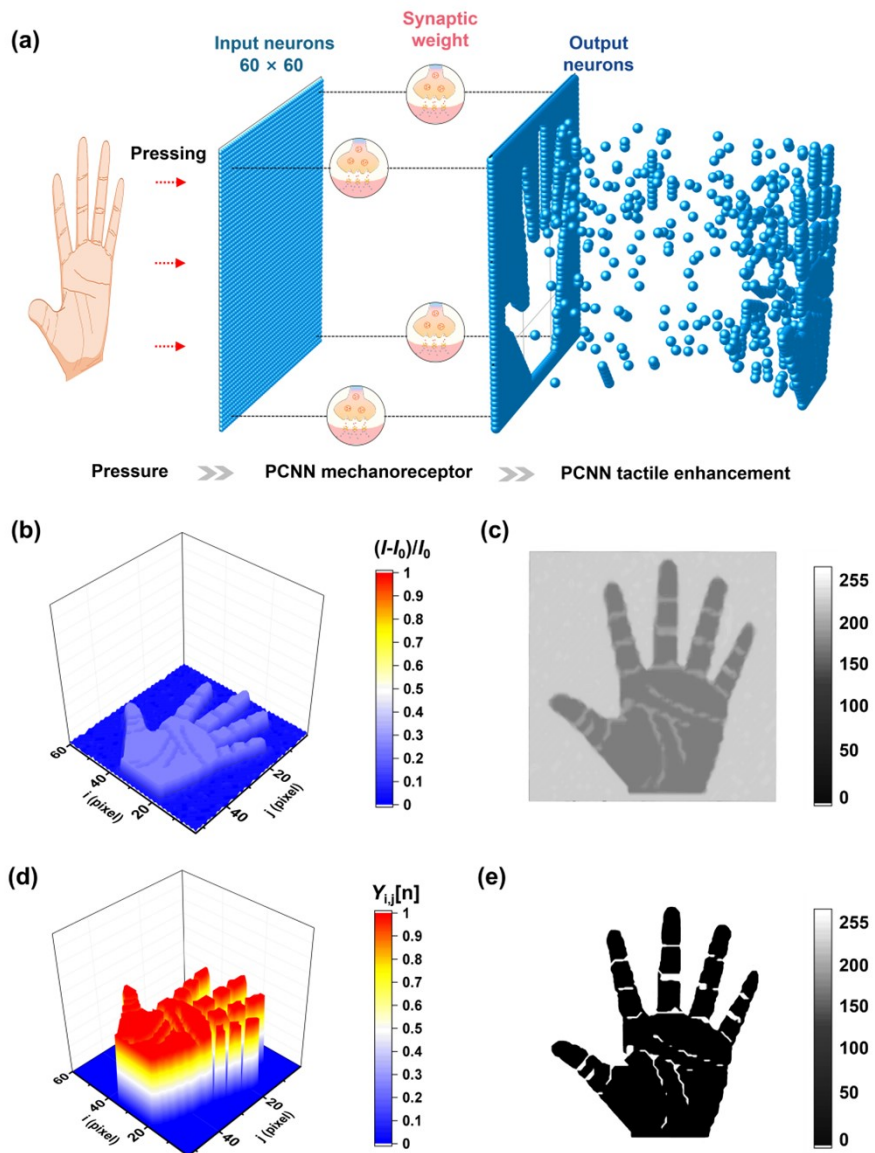


Fig. S32. (a) Schematic image demonstrating the 60×60 array based on **1** as mechanoreceptor for collecting initial palm texture, and PCNN model using to enhancing palm texture signal. (b) 3-D palm texture model obtained by 60×60 array based on **1**. (c) Initial 2-D palm texture gray image transformed by 3-D palm texture model. (d) Enhanced 3-D palm texture model obtained by 60×60 array based on **1**. (e) Enhanced 2-D palm texture gray image transformed by 3-D palm texture model.

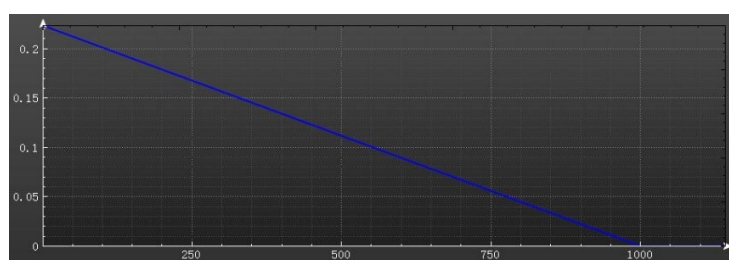


Fig. S33. Training curve of BPNN1 model, the ordinate value decreases to 0, suggesting the successful fitting of BPNN1 model.

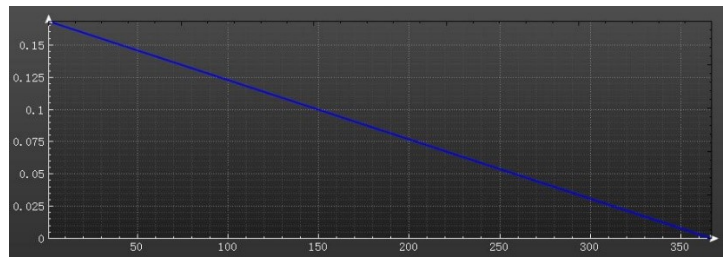


Fig. S34. Training curve of BPNN2 model, the ordinate value decreases to 0, suggesting the successful fitting of BPNN2 model.

Table S1. An overall comparison of this work and other works about luminescent mechanochromism polymer materials. (“Yes” outside the black circle means that this result is existent; “No” inside the black circle means that this result is non-existent; SMC: Stretched mechanochromism; BMC: Bended mechanochromism; PMC: Pressed mechanochromism)

Reference	This work	2	3	4	5	6	7	8
SMC	Yes	Yes	Yes	Yes	Yes	Yes	Yes	Yes
BMC	Yes	No						
PMC	Yes	No						
Human motion sensing	Yes	No	No	No	No	No	No	Yes
Hand gesture recognition	Yes	No						
Tactile enhanced palm Information collection	Yes	No						
Anti-counterfeiting	No	Yes	No	No	No	No	No	No
Bulging pressure sensing	No	Yes	No	No	No	No	No	No
Various color change	Yes	Yes	Yes	Yes	Yes	Yes	Yes	No
Finite element simulation	Yes	No	No	Yes	No	No	No	No

Reference

- [2] Q. Zhu and K. V. Vliet, N. Holten-Andersen, A. Miserez, *Adv. Funct. Mater.*, 2019, **29**, 1808191.
- [3] S. Zeng, D. Zhang, W. Huang, Z. Wang, S. G. Freire, X. Yu, A. T. Smith, E. Y. Huang, H. Nguon and L. Sun, *Nat. Commun.*, 2016, **7**, 11802.
- [4] M. Raisch, W. Maftuhin, M. Walter and M. Sommer, *Nat. Commun.*, 2021, **12**, 4243
- [5] S. Thazhathethil, T. Muramatsu, N. Tamaoki, C. Weder and Y. Sagara, *Angew. Chem.*, 2022, e202209225.
- [6] H. Hu, X. Cheng, Z. Ma, Rint P. Sijbesma and Z. Ma, *J. Am. Chem. Soc.*, 2022, **144**, 9971–9979.
- [7] Y. Sagara, M. Karman, E. Verde-Sesto, K. Matsuo, Y. Kim, N. Tamaoki and C. Weder, *J. Am. Chem. Soc.*, 2018, **140**, 1584–1587.
- [8] G. Lin, M. Si, L. Wang, S. Wei, W. Lu, H. Liu, Y. Zhang, D. Li and T. Chen, *Adv. Optical Mater.*, 2022, **10**, 2102306.

Table S2. The crystallographic data of HOF-TJ-1.

Crystal data	HOF-TJ-1
CCDC number	2210794
Crystal system	triclinic
Space group	P-1
Molecular formula	C38H51NO9
Formula weight	665.80
a / Å	9.7279(18)
b / Å	12.109(2)
c / Å	16.102(3)
α/°	87.019(7)
β/°	89.242(7)
γ/°	70.646(6)
Volume/ Å ³	1787.1(6)

Z	2
Density/ g/cm ³	1.237
GOF on F ²	1.041
R1a[>2σ()]	0.0843
ωR2b[>2σ()]	0.2186

Table S3. Summary of fluorescence decay lifetime of **1**.

Sample	λ_{ex} (nm)	λ_{em} (nm)	τ_1 (ns)	A_1	Percentag		Percentag		τ^*	χ^2
					e (%)	τ_2 (ns)	A_2	e (%)		
1	379	470	1.39	1143.05	51.62	14.12	63.16	48.38	5.97	1.074

$$[\tau^* = (A_1\tau_1 + A_2\tau_2)/(A_1\tau_1 + A_2\tau_2)]$$

Table S4. Element contents of C, Si, O, and N in porous HOF-TJ-1@PDMS film.

Elements	Wt%
C	54.12
Si	12.39
O	32.84
N	0.65
Total	100.00

Table S5. CIE coordinates of **1**, **2** and **3** with different stretched strains of 0, 20, 40, 60, 80 and 100% ($\lambda_{\text{ex}} = 365$ nm).

	1		2		3			
Strain (%)	x	y	Strain (%)	x	y	Strain (%)	x	y
0	0.1898	0.2079	0	0.1944	0.2515	0	0.1862	0.2471
20	0.2442	0.2214	20	0.2317	0.2943	20	0.1959	0.2691
40	0.2814	0.2298	40	0.2639	0.33	40	0.2025	0.3186
60	0.3424	0.2431	60	0.3003	0.3629	60	0.1998	0.3528
80	0.3816	0.2594	80	0.3213	0.3937	80	0.2109	0.412
100	0.4318	0.2659	100	0.3499	0.4153	100	0.239	0.4806

Table S6. Detection limits of **1–4** in stretching, bending and pressing process.

	Detection limit (DL)		
Sample	Stretching (%)	Bending (°)	Pressing (%)
1	0.00321	0.00227	1.191
2	0.201	0.0101	1.033
3	1.031	0.00504	2.812

4	0.598	0.0880	3.905
----------	-------	--------	-------

Table S7. CIE coordinates of **1**, **2** and **3** with different bending angles of 0, 30, 60, 90, 120, 150 and 180° ($\lambda_{\text{ex}} = 365 \text{ nm}$).

1			2			3		
Bending angle (°)	x	y	Bending angle (°)	x	y	Bending angle (°)	x	y
0	0.1898	0.2079	0	0.1944	0.2515	0	0.1862	0.2471
30	0.2532	0.2114	30	0.2054	0.2571	30	0.1929	0.2751
60	0.2814	0.2134	60	0.2267	0.2737	60	0.1962	0.326
90	0.3112	0.2231	90	0.2445	0.3048	90	0.2037	0.3666
120	0.3623	0.2351	120	0.2836	0.3605	120	0.2314	0.4388
150	0.4018	0.2378	150	0.3229	0.406	150	0.2391	0.4748
180	0.4421	0.2302	180	0.3686	0.4608	180	0.2441	0.4958

Table S8. CIE coordinates of **1** with different press strains of 0, 10, 20, 30 and 40%.

Strain (%)	x	y
0	0.2734	0.2154
10	0.2619	0.2064
20	0.2483	0.1964
30	0.2359	0.1904
40	0.2212	0.1869

Table S9. Summary of input and output information during the training of BPNN1 for classifying bending angle (θ_1).

Input (R/B value)	Output data (bending angle)				
	0°	30°	60°	90°	Curl up
0.19249	1	0	0	0	0
0.45532	0	1	0	0	0
0.62551	0	0	1	0	0
0.788	0	0	0	1	0
None	0	0	0	0	1

In [Table S9](#), all data is used to training the BPNN1. The R/B value as input information are inputted in the input column of the BPNN. Various “0” and “1” inputted into the output column of the BPNN, in which “0” represents the false test object, and “1” represents the correct test object. All data is used to train the BPNN1.

Table S10. Network structure information of BPNN1.

Network structure information		
Input layer	2 neurons	1 Paranoid
Hidden layer 1	6 neurons	1 Paranoid

Hidden layer 2	5 neurons			
Output layer	FANN_NETTYPE_LAYER			
Network type	FANN_TRAIN_RPROP			
Training function	FANN_ERRORFUNC_LINEAR			
Error function	FANN_STOPFUNC_MSE			
Termination function	FANN_SIGMOID_SYMMETRI C			
Hidden layer excitation function	FANN_SIGMOID_SYMMETRI C			
Output layer excitation function	FANN_NETTYPE_LAYER			
Network weight value				
Arrangement	Wire number	Output point (n)	Input point (m)	Weight value (W)
1	0	0	2	0.589033
	1	1	2	-1432.92
	2	0	3	21.6051
	3	1	3	6.67888
	4	0	4	0.991614
	5	1	4	-1432.92
	6	0	5	10.5879
	7	1	5	5.20038
	8	0	6	2.50251
	9	1	6	1.2668
	10	0	7	1.01827
	11	1	7	-1432.92
	12	2	9	1500
	13	3	9	1500
	14	4	9	1500
	15	5	9	1500
	16	6	9	1500
	17	7	9	1500
	18	8	9	1500
2	19	2	10	3.75024
	20	3	10	-50.6034
	21	4	10	4.6981
	22	5	10	169.414
	23	6	10	-124.586
	24	7	10	27.4439
	25	8	10	-3.58068
	26	2	11	2.50342
	27	3	11	-108.655
	28	4	11	6.24981
	29	5	11	91.0153
	30	6	11	38.6634
	31	7	11	31.4101
	32	8	11	-9.96034
	33	2	12	6.54752
	34	3	12	0.151122
	35	4	12	7.88862
	36	5	12	-63.3146
	37	6	12	83.0465
	38	7	12	6.76897
	39	8	12	-2.94446
	40	2	13	3.21999
	41	3	13	2.99298
	42	4	13	97.5685
	43	5	13	-4.07579

44	6	13	-232.888
45	7	13	9.16366
46	8	13	17.4696
Input / output column coefficients for manual calculation			
Listing		Minimum	Maximum
0°		0	1
30°		0	1
60°		0	1
90°		0	1
Curl up		0	1
Deviation statistics: mean variance			
Listing		All rows	Calculation line
0°		0	0
30°		0	0
60°		0	0
90°	5.18103e-07	5.18103e-07	0
Curl up	0	0	0

Table S11. The summary of mean square error (MSE), original value (OV), calculated value (CV), variance (Var.) for BPNN1.

1	Input item R/B	0° (MSE = 0)			30° (MSE = 0)			60° (MSE = 0)			90° (MSE = 5.18103e-07)			Curl up (MSE = 0)		
		OV	CV	Var	OV	CV	Var	OV	CV	Var	OV	CV.	Var.	OV	CV	Var
	
3	0.19249	1	1	0	0	0	0	0	0	0	0.000118	1.3924e-08	0	0	0	
4	0.45532	0	0	0	1	1	0	0	0	0	0	0	0	0	0	0
5	0.62551	0	0	0	0	0	0	1	1	0	0	0.000542	2.93764e-07	0	0	0
6	0.788	0	0	0	0	0	0	0	0	0	0.998683	1.73449e-06	0	0	0	
7	None	0	0	0	0	0	0	0	0	0	0.0007405	5.4834e-07	1	1	0	

In Table S11, all data is utilized to test the BPNN1. The R/B value as input information are inputted in the input column of the BPNN1. Through the BPNN1 calculation, various values (0-1) can be outputted, in which the values close to “0” represents the false test object, the values close to “1” represents the correct test object. By comparing the OV with CV, the variance can be obtained, which suggests that the BPNN1 has a good accuracy for classifying bending angle (θ_1).

Table S12. The matlab code of this BPNN 1.

Matlab code
<pre>function [f00, f01, f02, f03, f04] = MPredict(f10) f10 = (f10 - (0 + 5.4259368421052629) / 2.0) /(5.4259368421052629 - (0 + 5.4259368421052629) / 2.0); fWei0 = 0.589033; fWei1 = -1432.92; fWei2 = 21.6051; fWei3 = 6.67888; fWei4 = 0.991614; fWei5 = -1432.92; fWei6 = 10.5879; fWei7 = 5.20038; fWei8 = 2.50251; fWei9 = 1.2668; fWei10 = 1.01827;</pre>

```
fWei11 = -1432.92;
fWei12 = 1500;
fWei13 = 1500;
fWei14 = 1500;
fWei15 = 1500;
fWei16 = 1500;
fWei17 = 1500;
fWei18 = 1500;
fWei19 = 3.75024;
fWei20 = -50.6034;
fWei21 = 4.6981;
fWei22 = 169.414;
fWei23 = -124.586;
fWei24 = 27.4439;
fWei25 = -3.58068;
fWei26 = 2.50342;
fWei27 = -108.655;
fWei28 = 6.24981;
fWei29 = 91.0153;
fWei30 = 38.6634;
fWei31 = 31.4101;
fWei32 = -9.96034;
fWei33 = 6.54752;
fWei34 = 0.151122;
fWei35 = 7.88862;
fWei36 = -63.3146;
fWei37 = 83.0465;
fWei38 = 6.76897;
fWei39 = -2.94446;
fWei40 = 3.21999;
fWei41 = 2.99298;
fWei42 = 97.5685;
fWei43 = -4.07579;
fWei44 = -232.888;
fWei45 = 9.16366;
fWei46 = 17.4696;
f0 = f10;
f1 = 1.0;
f2 = 0.0;
f3 = 0.0;
f4 = 0.0;
f5 = 0.0;
f6 = 0.0;
f7 = 0.0;
f2 = f2 + f0 * fWei0;
f2 = f2 + f1 * fWei1;
f2 = f2 * 0.5;
f2 = (2.0 / (1.0 + exp(-2.0 * f2))- 1.0);
f3 = f3 + f0 * fWei2;
f3 = f3 + f1 * fWei3;
f3 = f3 * 0.5;
f3 = (2.0 / (1.0 + exp(-2.0 * f3))- 1.0);
f4 = f4 + f0 * fWei4;
f4 = f4 + f1 * fWei5;
f4 = f4 * 0.5;
f4 = (2.0 / (1.0 + exp(-2.0 * f4))- 1.0);
f5 = f5 + f0 * fWei6;
```

```
f5 = f5 + f1 * fWei7;
f5 = f5 * 0.5;
f5 = (2.0 / (1.0 + exp(-2.0 * f5))- 1.0);
f6 = f6 + f0 * fWei8;
f6 = f6 + f1 * fWei9;
f6 = f6 * 0.5;
f6 = (2.0 / (1.0 + exp(-2.0 * f6))- 1.0);
f7 = f7 + f0 * fWei10;
f7 = f7 + f1 * fWei11;
f7 = f7 * 0.5;
f7 = (2.0 / (1.0 + exp(-2.0 * f7))- 1.0);
f8 = 1.0;
f9 = 0.0;
f10 = 0.0;
f11 = 0.0;
f12 = 0.0;
f13 = 0.0;
f9 = f9 + f2 * fWei12;
f9 = f9 + f3 * fWei13;
f9 = f9 + f4 * fWei14;
f9 = f9 + f5 * fWei15;
f9 = f9 + f6 * fWei16;
f9 = f9 + f7 * fWei17;
f9 = f9 + f8 * fWei18;
f9 = f9 * 0.5;
f9 = (2.0 / (1.0 + exp(-2.0 * f9))- 1.0);
f10 = f10 + f2 * fWei19;
f10 = f10 + f3 * fWei20;
f10 = f10 + f4 * fWei21;
f10 = f10 + f5 * fWei22;
f10 = f10 + f6 * fWei23;
f10 = f10 + f7 * fWei24;
f10 = f10 + f8 * fWei25;
f10 = f10 * 0.5;
f10 = (2.0 / (1.0 + exp(-2.0 * f10))- 1.0);
f11 = f11 + f2 * fWei26;
f11 = f11 + f3 * fWei27;
f11 = f11 + f4 * fWei28;
f11 = f11 + f5 * fWei29;
f11 = f11 + f6 * fWei30;
f11 = f11 + f7 * fWei31;
f11 = f11 + f8 * fWei32;
f11 = f11 * 0.5;
f11 = (2.0 / (1.0 + exp(-2.0 * f11))- 1.0);
f12 = f12 + f2 * fWei33;
f12 = f12 + f3 * fWei34;
f12 = f12 + f4 * fWei35;
f12 = f12 + f5 * fWei36;
f12 = f12 + f6 * fWei37;
f12 = f12 + f7 * fWei38;
f12 = f12 + f8 * fWei39;
f12 = f12 * 0.5;
f12 = (2.0 / (1.0 + exp(-2.0 * f12))- 1.0);
f13 = f13 + f2 * fWei40;
f13 = f13 + f3 * fWei41;
f13 = f13 + f4 * fWei42;
f13 = f13 + f5 * fWei43;
```

```

f13 = f13 + f6 * fWei44;
f13 = f13 + f7 * fWei45;
f13 = f13 + f8 * fWei46;
f13 = f13 * 0.5;
f13 = (2.0 / (1.0 + exp(-2.0 * f13))- 1.0);
f00 = f9;
f01 = f10;
f02 = f11;
f03 = f12;
f04 = f13;
f00 = f00 * (1 - (0 + 1) / 2.0) + (0 + 1) / 2.0;
f01 = f01 * (1 - (0 + 1) / 2.0) + (0 + 1) / 2.0;
f02 = f02 * (1 - (0 + 1) / 2.0) + (0 + 1) / 2.0;
f03 = f03 * (1 - (0 + 1) / 2.0) + (0 + 1) / 2.0;
f04 = f04 * (1 - (0 + 1) / 2.0) + (0 + 1) / 2.0;

```

Table S13. Summary of input and output information during the training of BPNN2.

Input (θ_1 and θ_2)		Output data (θ_1 - θ_2)				
θ_1	θ_2	θ_1 -left45°	θ_1 -left90°	θ_1 -right45°	θ_1 -right90°	θ_1 -none
θ1	left45°	1	0	0	0	0
θ1	left90°	0	1	0	0	0
θ1	right45°	0	0	1	0	0
θ1	right90°	0	0	0	1	0
θ1	none	0	0	0	0	1

In Table S13, all data is used to training the BPNN2. The θ_1 and θ_2 values of finger as input information are inputted in the input column of the BPNN2. Various “0” and “1” inputted into the output column of the BPNN2, in which “0” represents the false angle, and “1” represents the correct angle. All data is used to train the BPNN2.

Table S14. Network structure information of BPNN2.

Network structure information		
Input layer	3 neurons	1 Paranoid
Hidden layer 1	6 neurons	1 Paranoid
Hidden layer 2	5 neurons	
Output layer	FANN_NETTYPE_LAYER	
Network type	FANN_TRAIN_RPROP	
Training function	FANN_ERRORFUNC_LINEAR	
Error function	FANN_STOPFUNC_MSE	
Termination function	FANN_SIGMOID_SYMMETRIC	
Hidden layer excitation function	FANN_SIGMOID_SYMMETRIC	

Network weight value				
Arrangement	Arrangement	Arrangement	Arrangement	Arrangement
1	0	0	3	0.403499
	1	1	3	1.75701
	2	2	3	0.414392
	3	0	4	670.918
	4	1	4	-1149.08
	5	2	4	-454.169
	6	0	5	2.13783
	7	1	5	-4.81258
	8	2	5	-0.227264

	9	0	6	2.00292
	10	1	6	0.13086
	11	2	6	0.0903639
	12	0	7	1499.25
	13	1	7	-2.33014
	14	2	7	-1498.15
	15	0	8	0.401937
	16	1	8	9.21087
	17	2	8	0.780127
	18	3	10	302.478
	19	4	10	941.381
	20	5	10	1500
	21	6	10	302.57
	22	7	10	736.368
	23	8	10	733.574
	24	9	10	1500
	25	3	11	3.56259
	26	4	11	6.43238
	27	5	11	-20.9773
	28	6	11	5.3754
	29	7	11	9.65955
	30	8	11	-37.0324
	31	9	11	-5.95667
	32	3	12	-10.4143
	33	4	12	12.8387
	34	5	12	-55.511
2	35	6	12	1.73649
	36	7	12	12.9916
	37	8	12	-25.4246
	38	9	12	-8.79665
	39	3	13	-50.8769
	40	4	13	3.92762
	41	5	13	-1.21771
	42	6	13	1.68703
	43	7	13	4.33599
	44	8	13	34.6841
	45	9	13	-0.447542
	46	3	14	142.733
	47	4	14	6.10909
	48	5	14	2.47398
	49	6	14	109.29
	50	7	14	1.2797
	51	8	14	19.4559
	52	9	14	-1.60489

Input / output column coefficients for manual calculation

Listing	Listing	Listing	Listing	Listing
0	1			
0.95	5.26316			
0	1			
0	1			
0	1			
0	1			

Deviation statistics: mean variance

Listing	Listing	Listing	Listing	Listing
2.35445e-07	2.35445e-07	0		
1.10528e-07	1.10528e-07	0		

	3.34785e-09	3.34785e-09	0
	3.30856e-07	3.30856e-07	0
	0	0	0

Table S15. The summary of mean square error (MSE), original value (OV), calculated value (CV), variance (Var.) of BPNN2.

1	Input item	θ1-left45 (MSE = 2.35445e-07)			θ1-left90 (MSE = 1.10528e-07)			θ1-right45 (MSE = 3.34785e-09)			θ1-right90 (MSE = 3.30856e-07)			θ1-none (MSE = 0)			
		θ1 and θ2	OV.	CV.	Var.	θ1	OV.	CV.	Var.	θ1	OV.	CV.	Var.	θ1	OV.	CV.	Var.
3	θ1 left45	1	0.998915	1.17723e-06	0	0.000316	9.9856e-08	0	0	0	0	4.85e-05	2.35225e-09	0	0	0	0
4	θ1 left90	0	0	0	1	0.99938	3.844e-07	0	6.1e-05	3.721e-09	0	0	0	0	0	0	0
5	θ1 right45	0	0	0	0	0.0002615	6.83823e-08	1	0.999893	1.1449e-08	0	0.000222	4.9284e-08	0	0	0	0
6	θ1 right90	0	0	0	0	0	0	0	3.95e-05	1.56025e-09	1	0.999008	9.84064e-07	0	0	0	0
7	θ1 none	0	0	0	0	0	0	0	3e-06	9e-12	0	0.0007865	6.18582e-07	1	1	0	0
8	θ1 left45	1	0.998915	1.17723e-06	0	0.000316	9.9856e-08	0	0	0	0	4.85e-05	2.35225e-09	0	0	0	0

In [Table S15](#), all data is utilized to test the BPNN2. The θ_1 and θ_2 values of finger as input information are inputted in the input column of the BPNN2. Through the BPNN2 calculation, various values (0-1) can be outputted, in which the values close to “0” represents the false angle, the values close to “1” represents the correct angle. By comparing the OV with CV, the variance can be obtained, which suggests that the BPNN2 has a good accuracy for sensing sensing and rotating angles.

Table S16. The matlab code of this BPNN2.

Matlab code
<pre> function [f00, f01, f02, f03, f04] = MPredict(f10, f11) f10 = (f10 - (0 + 1) / 2.0) / (1 - (0 + 1) / 2.0); f11 = (f11 - (0.95 + 5.2631578947368425) / 2.0) / (5.2631578947368425 - (0.95 + 5.2631578947368425) / 2.0); fWei0 = 0.403499; fWei1 = 1.75701; fWei2 = 0.414392; fWei3 = 670.918; fWei4 = -1149.08; fWei5 = -454.169; fWei6 = 2.13783; fWei7 = -4.81258; fWei8 = -0.227264; fWei9 = 2.00292; fWei10 = 0.13086; fWei11 = 0.0903639; fWei12 = 1499.25; fWei13 = -2.33014; fWei14 = -1498.15; fWei15 = 0.401937; fWei16 = 9.21087; fWei17 = 0.780127; fWei18 = 302.478; fWei19 = 941.381; fWei20 = 1500; fWei21 = 302.57; </pre>

```
fWei22 = 736.368;
fWei23 = 733.574;
fWei24 = 1500;
fWei25 = 3.56259;
fWei26 = 6.43238;
fWei27 = -20.9773;
fWei28 = 5.3754;
fWei29 = 9.65955;
fWei30 = -37.0324;
fWei31 = -5.95667;
fWei32 = -10.4143;
fWei33 = 12.8387;
fWei34 = -55.511;
fWei35 = 1.73649;
fWei36 = 12.9916;
fWei37 = -25.4246;
fWei38 = -8.79665;
fWei39 = -50.8769;
fWei40 = 3.92762;
fWei41 = -1.21771;
fWei42 = 1.68703;
fWei43 = 4.33599;
fWei44 = 34.6841;
fWei45 = -0.447542;
fWei46 = 142.733;
fWei47 = 6.10909;
fWei48 = 2.47398;
fWei49 = 109.29;
fWei50 = 1.2797;
fWei51 = 19.4559;
fWei52 = -1.60489;
f0 = fI0;
f1 = fI1;
f2 = 1.0;
f3 = 0.0;
f4 = 0.0;
f5 = 0.0;
f6 = 0.0;
f7 = 0.0;
f8 = 0.0;
f3 = f3 + f0 * fWei0;
f3 = f3 + f1 * fWei1;
f3 = f3 + f2 * fWei2;
f3 = f3 * 0.5;
f3 = (2.0 / (1.0 + exp(-2.0 * f3))- 1.0);
f4 = f4 + f0 * fWei3;
f4 = f4 + f1 * fWei4;
f4 = f4 + f2 * fWei5;
f4 = f4 * 0.5;
f4 = (2.0 / (1.0 + exp(-2.0 * f4))- 1.0);
f5 = f5 + f0 * fWei6;
f5 = f5 + f1 * fWei7;
f5 = f5 + f2 * fWei8;
f5 = f5 * 0.5;
f5 = (2.0 / (1.0 + exp(-2.0 * f5))- 1.0);
f6 = f6 + f0 * fWei9;
f6 = f6 + f1 * fWei10;
```

```
f6 = f6 + f2 * fWei11;
f6 = f6 * 0.5;
f6 = (2.0 / (1.0 + exp(-2.0 * f6))- 1.0);
f7 = f7 + f0 * fWei12;
f7 = f7 + f1 * fWei13;
f7 = f7 + f2 * fWei14;
f7 = f7 * 0.5;
f7 = (2.0 / (1.0 + exp(-2.0 * f7))- 1.0);
f8 = f8 + f0 * fWei15;
f8 = f8 + f1 * fWei16;
f8 = f8 + f2 * fWei17;
f8 = f8 * 0.5;
f8 = (2.0 / (1.0 + exp(-2.0 * f8))- 1.0);
f9 = 1.0;
f10 = 0.0;
f11 = 0.0;
f12 = 0.0;
f13 = 0.0;
f14 = 0.0;
f10 = f10 + f3 * fWei18;
f10 = f10 + f4 * fWei19;
f10 = f10 + f5 * fWei20;
f10 = f10 + f6 * fWei21;
f10 = f10 + f7 * fWei22;
f10 = f10 + f8 * fWei23;
f10 = f10 + f9 * fWei24;
f10 = f10 * 0.5;
f10 = (2.0 / (1.0 + exp(-2.0 * f10))- 1.0);
f11 = f11 + f3 * fWei25;
f11 = f11 + f4 * fWei26;
f11 = f11 + f5 * fWei27;
f11 = f11 + f6 * fWei28;
f11 = f11 + f7 * fWei29;
f11 = f11 + f8 * fWei30;
f11 = f11 + f9 * fWei31;
f11 = f11 * 0.5;
f11 = (2.0 / (1.0 + exp(-2.0 * f11))- 1.0);
f12 = f12 + f3 * fWei32;
f12 = f12 + f4 * fWei33;
f12 = f12 + f5 * fWei34;
f12 = f12 + f6 * fWei35;
f12 = f12 + f7 * fWei36;
f12 = f12 + f8 * fWei37;
f12 = f12 + f9 * fWei38;
f12 = f12 * 0.5;
f12 = (2.0 / (1.0 + exp(-2.0 * f12))- 1.0);
f13 = f13 + f3 * fWei39;
f13 = f13 + f4 * fWei40;
f13 = f13 + f5 * fWei41;
f13 = f13 + f6 * fWei42;
f13 = f13 + f7 * fWei43;
f13 = f13 + f8 * fWei44;
f13 = f13 + f9 * fWei45;
f13 = f13 * 0.5;
f13 = (2.0 / (1.0 + exp(-2.0 * f13))- 1.0);
f14 = f14 + f3 * fWei46;
f14 = f14 + f4 * fWei47;
```

```

f14 = f14 + f5 * fWei48;
f14 = f14 + f6 * fWei49;
f14 = f14 + f7 * fWei50;
f14 = f14 + f8 * fWei51;
f14 = f14 + f9 * fWei52;
f14 = f14 * 0.5;
f14 = (2.0 / (1.0 + exp(-2.0 * f14))) - 1.0);
f00 = f10;
f01 = f11;
f02 = f12;
f03 = f13;
f04 = f14;
f00 = f00 * (1 - (0 + 1) / 2.0) + (0 + 1) / 2.0;
f01 = f01 * (1 - (0 + 1) / 2.0) + (0 + 1) / 2.0;
f02 = f02 * (1 - (0 + 1) / 2.0) + (0 + 1) / 2.0;
f03 = f03 * (1 - (0 + 1) / 2.0) + (0 + 1) / 2.0;
f04 = f04 * (1 - (0 + 1) / 2.0) + (0 + 1) / 2.0;

```

Table S17. Summary data of the initial 3-D fingerprint texture image before tactile enhancement.

Table S18. Summary data of the initial 2-D fingerprint texture gray image before tactile enhancement.

Table S19. Summary data of the 3-D fingerprint texture image after tactile enhancement.

Table S20. Summary data of the 2-D fingerprint texture gray image after tactile enhancement.

Table S21. Summary data of the 3-D palm texture image before tactile enhancement.

A grayscale heatmap visualization of a sparse matrix. The matrix consists of a grid of small black squares on a white background. These black squares are scattered across the entire area, representing non-zero elements in a large matrix. The distribution is relatively uniform, though there are some slight vertical and horizontal clustering of the data points.

Table S22. Summary data of the initial 2-D palm texture gray image before tactile enhancement.

Table S23. Summary data of the 3-D palm texture image after tactile enhancement.

Table S24. Summary data of the 3-D palm texture gray image after tactile enhancement.

